Chapter 5
Switching Dynamics of a Surface Stabilized Ferroelectric Liquid Crystal Mixture

Flat panel displays with ferroelectric liquid crystals (FLCs) could potentially provide the advantages of fast response, bi-stability and wide viewing angle.[3,76] The memory-like behavior of FLC materials also opens up new possibilities in their applications. However, the design of new FLC materials often proves frustrating since it is necessary to obtain a material with both a chiral structure and a smectic C* (SmC*) phase. Although the former is often achievable by synthesis, the latter has seemed more a matter of luck. For practical applications a wide thermodynamically stable SmC* phase is generally required. A method for broadening the temperature range of thermodynamically stable C* phases is to obtain a eutectic by mixing several LC components. The design of new FLC components is therefore simplified to doping of chiral compounds into a mixture with a wide thermodynamically stable SmC phase.[77] This approach gains significance in view of the fact that all commercial FLC materials are mixtures. The properties imparted to a mixture by the addition of chiral components are more relevant to applications than are its properties as the neat liquid.

For the interests of both fundamental research and industrial applications, many efforts have been made to investigate the switching behavior of FLC material.[74,78,79] It is important to note that upon the reversal of the sign of an applied field, all the molecules in the ferroelectric phases switch by rotation about a tilt cone. This is basically because coupling with the applied field is through

ferroelectric spontaneous polarization, not through coupling with any individual molecular dipoles. An understanding of the switching dynamics of FLC mixtures is therefore useful, not only for the development of novel flat panel displays, but also for the design of new FLC materials.

During the past decade, time-resolved Fourier transform infrared absorption spectroscopy (trFTIR) had been shown to be a powerful tool for the investigation of orientational and conformational dynamics in complex molecular systems.[22,25,26,80] This chapter describes some interesting results on the switching dynamics of a surface stabilized FLC (SSFLC) mixture by combining trFTIR with second harmonic generation and time-resolved electro-optical (EO) measurements.

5.1. Experimental Procedures

The SSFLC cells used consist of two CaF_2 plates coated with indium tin oxide (ITO) conducting films and polyimide alignment layers rubbed unidirectionally. The substrates were assembled in a homogeneous geometry with a 2-μm cell thickness to result in a surface stabilized structure. The cell thickness is close to the half-wave thickness of $d_{\lambda/2} = \lambda/(2 \cdot \Delta n) = 1.9 \mu m$ with $\Delta n = 0.17$ and $\lambda = 0.633 \mu m$.

A chevron-mode ferroelectric liquid crystal mixture FELIX 017/100 from Clariant was filled into a test cell at a temperature above the isotropic phase of the FLC mixture. This material is a mixture of homologous, with a fairly wide SmC* range from 73 °C to –28 °C, and is promising for flat panel display applications. The test cells were slowly cooled to 35 °C and then inserted into a pair of cross polarizers. All our SSFLC cells appear single domain examined with a polarizing microscope.

For probing the electro-optical properties of the SSFLC cells, bipolar square-wave voltage pulses were applied and the optical transmission was measured as a function of time and rotation angle of the test cell about the optical beam propagation direction. A helium-neon laser with a wavelength of 632.8 nm was used.

FTIR spectra from 900 to 3500 cm^{-1} with 8 cm^{-1} resolution were recorded with an Oriel MIR-8000 FTIR spectrometer equipped with a liquid nitrogen cooled HgCdTe detector. A bipolar square-wave pulse, similar to that in the EO measurements, was applied to excite the SSFLC cells during the trFTIR measurement.[5]

The Second Harmonic Generation (SHG) signals of the SSFLC cell were measured by a pump beam with a wavelength of 1.06 μm, which is the output of a Q-switched Nd-YAG laser. The pulse duration of the pump beam is about 8 ns. A photomultiply tube equipped with a monochromator was used as the detector to record the SHG signal with a wavelength of 532 nm. Suitable polarization combinations of the pump beam and SHG signal were controlled with a pair of polarizers. The timing between the laser probing and the electrical driving field on the SSFLC cell was controlled with a combination of function generator and digital delay generator.

5.2. Second Harmonic Generation and Polarized FTIR Absorption Spectroscopy of an SSFLC

The azimuthal absorption pattern of an infrared beam propagating through a sample can be expressed as[72]

$$A(\Phi) = \frac{N\pi}{3c} \int [\mu_g^{(K)} \cdot \hat{E}_{IR}]^2 \, f(\Omega) \, d\Omega \qquad (5.1)$$

where N denotes the number density of the Kth IR dipole moment $\mu_g^{(K)} = \partial \mu_g / \partial Q_K$, Φ is the angle between the incident infrared polarization E_{IR} and the laboratory X-axis, and $f(\Omega)$ represents the orientation distribution of $\mu_g^{(K)}$. For normal incidence on the XY plane (see Fig. 5.1), the integrated absorbance by an atomic group with IR dipole moment parallel to the molecular long axis (β=0) can be expressed as

$$A(\Phi) = (\cos\theta \cos\Phi + \cos\phi \sin\theta \sin\Phi)^2 \qquad (5.2)$$

where θ denotes the cone angle of FLC, and ϕ the azimuthal angle of molecular long axis relative to the layer normal X_1. The chevron angle δ of the SSFLC is small and can be neglected in this discussion without causing significant difference. For an atomic group with IR dipole moment parallel or perpendicular to the molecular long axis, the equations for the azimuthal pattern of integrated IR absorbance can be simplified to be

$$A(\Phi)=\begin{cases}\dfrac{1}{2}\sin^2(\Phi\mp\theta), & \phi=\begin{cases}0\\ \pi\end{cases}\\ \dfrac{1}{8}[3-\cos(2\theta)-2\cos^2\theta\cos(2\Phi)], & \phi=\dfrac{\pi}{2}\end{cases} \tag{5.3}$$

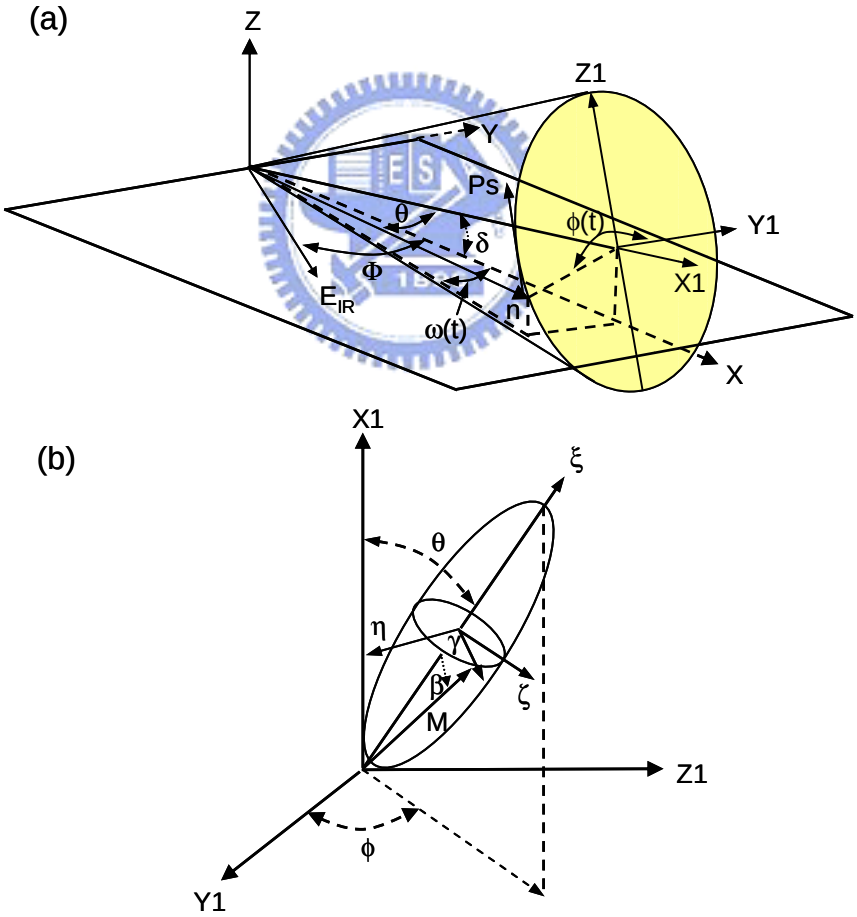

FIG. 5.1. Schematic diagram showing the relationship among the molecular frame (ξηζ), layer frame ($X_1Y_1Z_1$) and laboratory coordinates system (XYZ).

Figure 5.2 presents the calculated IR absorbance patterns for parallel and perpendicular infrared dipole moments. Within the calculation we assume the IR dipoles to be collectively rotated along the layer normal from $\phi = 0$ to π by changing polarity of the applied field. Note that the angular shift of the azimuthal patterns is about twice the apparent cone angle.

The SSFLC structure shown in Fig. 5.1 exhibits a C_2 symmetry with the C_2–axis along the Z-axis. The non-vanishing second-order non-linear optical susceptibility components are: $\chi^{(2)}_{ZZZ}$, $\chi^{(2)}_{XXZ} = \chi^{(2)}_{XZX} = \chi^{(2)}_{ZXX}$, $\chi^{(2)}_{YYZ} = \chi^{(2)}_{YZY} = \chi^{(2)}_{ZYY}$, $\chi^{(2)}_{XYZ} = \chi^{(2)}_{YXZ}$, $\chi^{(2)}_{XZY} = \chi^{(2)}_{ZXY}$, $\chi^{(2)}_{YZX} = \chi^{(2)}_{ZYX}$. We can calculate optical second-harmonic signal with[81]

$$I_{2\omega} = I_{\omega}^{2} \left| \hat{e}_{2\omega} \cdot \chi^{(2)} : \hat{e}_{\omega} \hat{e}_{\omega} \right|^{2} \tag{5.4}$$

For a rod-shaped FLC molecule, we assume that there is a single dominant nonlinear polarizability component along the molecular long axis. From Eq. (5.4), we note that the chevron FLC structure can not generate SHG signal at normal incidence.[82] SH azimuthal patterns with various optical polarization combinations were therefore calculated by using geometry with an inclined incidence, with the X-axis being along the cell rubbing direction. The results with an SSFLC at $\varphi = \pi/2$ are presented in Fig. 5.3. No *s*-polarized SH output can be generated when the cell is excited with an *s*-polarized fundamental beam. SHG activity also disappears in an SSFLC at $\varphi = 0°$ or 180°.

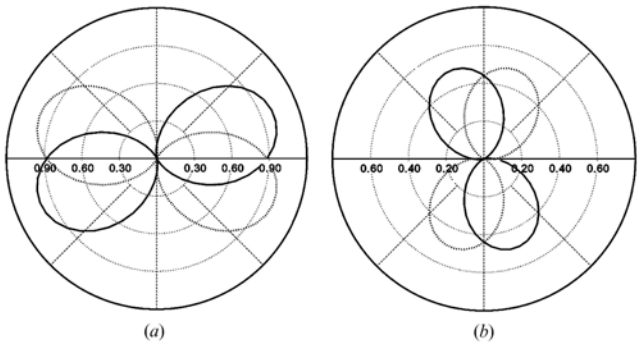

FIG. 5.2. Theoretical curves of the azimuthal FTIR patterns with (a) IR dipole moment pointing to $\beta = 0°$ or (b) $\beta = 90°$ of an SSFLC. Here ϕ of the dipole moment is assumed to be 0° (dashed curve) or 180° (solid).

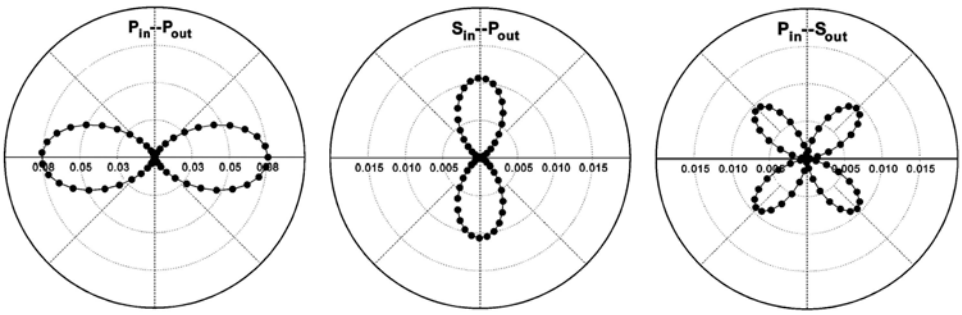

FIG. 5.3. Theoretical curves of azimuthal patterns of second harmonic generation for an SSFLC cell with various optical beam polarization combinations.

5.3. Results and Discussion

5.3.1. Steady-State Properties of an SSFLC

An SSFLC cell was prepared and characterized with infrared absorption spectroscopy; the results are shown in Fig. 5.4. We shall emphasize that these IR absorption peaks are contributed from multiple molecular species of the FLC mixture. The observed simplicity of each IR absorption line profile indicates that these molecular species possess high structural similarity. If IR dipoles from different FLC species are not aligned, the resulting azimuthal pattern for each IR absorption line shall reveal no clear azimuthal anisotropy. This is also true in a field-induced reorientation process. A clear time-resolved FTIR azimuthal anisotropy shall indicate a correlated movement of IR dipoles among different FLC species. Therefore a FTIR study on an FLC mixture should yield useful information about the inter-species alignment and field-induced reorientation dynamics which is not available from a study with neat FLC.

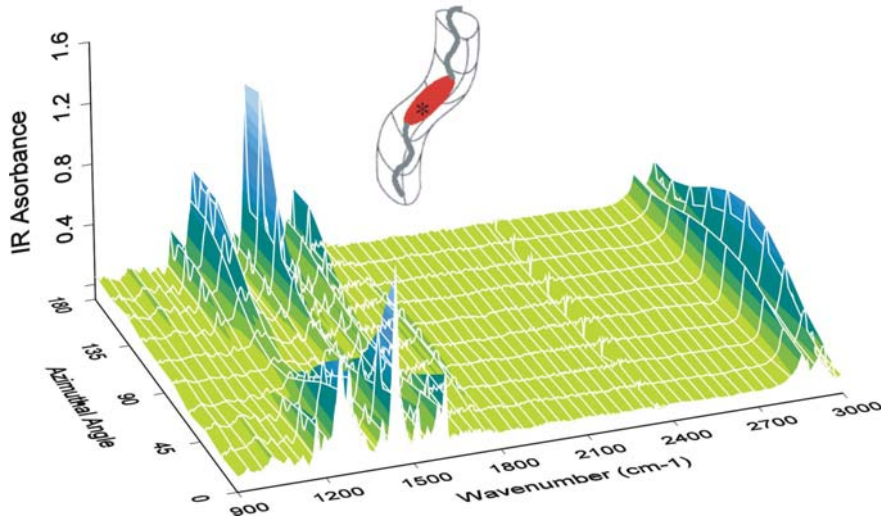

FIG. 5.4. FTIR spectra of an SSFLC measured without applied electric field, plotted as a function of the angle between the incident IR polarization and the rubbing direction of the cell (i.e., the X-axis).

Our objective in this study is to determine whether the molecular fragments of different FLC species in an FLC mixture move correlatively in a steady dc field or during a field-induced reorientation process. For this purpose, we categorize the observed FTIR absorption lines into two groups: the FLC core modes and modes associated with flexible alkyl chains. To help further discussion, an effective medium picture with a schematic molecular structure is presented in the inset of Fig. 5.4. The schematic structure is distinguished with a rigid core part and flexible alkyl chains. The major features of the IR spectra shown in Fig. 5.4, which originate from normal modes associated with the FLC cores, are at 1169, 1250, 1439, 1516, 1608, and 1763 cm^{-1}; and those from the alkyl chains are at 2851 and 2924 cm^{-1}.[83] The highest two peaks at 2851 and 2924 cm^{-1} are attributed to the symmetric and anti-symmetric CH_2 stretching along the alkyl chains of the FLC molecules. The peak at 1763 cm^{-1} is due to the C=O stretching, and the features at 1608 and 1516 cm^{-1} are mainly from the C–C stretching of the FLC core. The 1439 cm^{-1} peak arises from the combination of the C–C stretch and the in-plane wag of the C–H on the FLC core. The remaining normal modes at 1169 and 1250 cm^{-1} are associated with the C–O–C motion of the FLC cores.

In Fig. 5.4, the rubbing direction of the SSFLC cell is aligned with $\Phi = 0°$. The measured azimuthal patterns show that the IR polarizations, which yield maximum absorption by functional groups associated with the FLC core, are all parallel to the averaged molecular long axis. However, for C–O and CH_2 groups the maximum IR absorption occurs with the IR polarization being perpendicular to the averaged molecular long axis. A similar result had also been observed on neat FLC materials.[84] The mutual orthogonality between the azimuthal patterns of IR absorption peaks from the core and alkyl chains can also be observed in the field-free state.

From Eqs. (5.2) and (5.3) we note that, without an applied field, the averaged molecular long axis should lie on the XZ-plane with $\Phi = \pi/2$.[85,86] When an electric field is applied, the averaged molecular long axis can rotate from the XZ-plane to $\Phi = 0$ or π depending on the polarity of the applied voltage. The resulting azimuthal patterns from each IR dipole are presented in Fig. 5.5. The Table 5.1 lists the deduced dichroic ratios $D = A_{\parallel} / A_{\perp}$ and the angular shift of azimuthal patterns by the electric field. Note that with a positive applied field the dichroic ratio for IR absorption by molecular segments associated with the FLC core is larger than that with a negative applied field. This suggests that the orientation distributions of these atomic groups are more ordered with a positive voltage than with a negative voltage. For these FLC core groups, the observed angular shifts of the azimuthal patterns are fairly close to the effective cone angle of the FLC medium (~28°) as shown by Eq. (5.2). For CH_2 groups, the dichroic ratios with positive and negative voltages are small and nearly identical. The IR absorption patterns shift only 21° from +5 to –5 V, reflecting a flexible and less ordered alignment than the core groups. With a given applied voltage, all core group azimuthal patterns form approximately a single pattern, which indicates that none of these atomic groups change their relative orientation in the steady-state alignments with a dc voltage of opposite polarity. This also appears to be true for CO and CH_2 groups. This is an interesting result considering that each observed IR

absorption peak can originate from atomic groups, which may belong to different FLC species, and thus strongly supports that the molecular fragments in the FLC mixture are aligned in unison with a dc field.

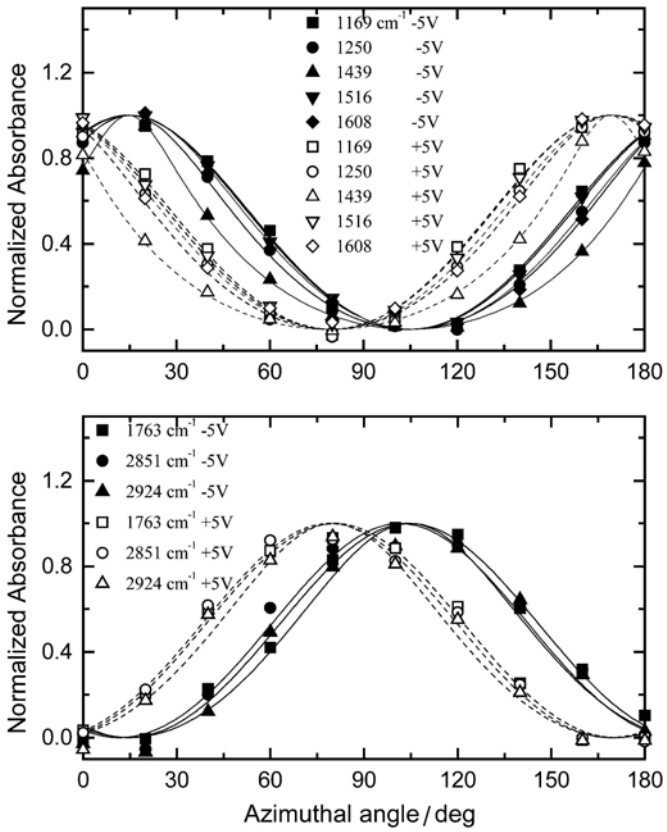

FIG. 5.5. Normalized IR azimuthal patterns of various atomic groups associated with the FLC core (upper), and the alkyl chains and C–O moiety (lower) are presented. Curves with solid symbols are the azimuthal patterns obtained with *negative* voltage while open symbols indicate the result with *positive* voltage.

The model of all FLC species rotating in unison can also be used to describe second harmonic generation. We note that the second harmonic intensity from our SSFLC cell is fairly weak at normal incidence.[82] In order to yield a better SH azimuthal anisotropy we fix the incident angle of the fundamental beam to be about 15°. The resulting SH azimuthal patterns are presented in Fig. 5.6 without applying an electric field. The measured SHG patterns qualitatively agree with calculated curves shown in Fig. 5.3. The non-vanishing s-in/s-out SH intensity and

asymmetric pattern with p-in/s-out suggest that the C_2 symmetry in our SSFLC may be partially broken.

As shown in the theoretical analysis, SHG activity from an SSFLC with $\Phi = 0°$ or 180° disappears with a maximum SHG signal occurring at $\Phi = \pi/2$. By rotating all FLC species in unison from $\Phi = 0°$ to 180° with a triangular wave form, we found that the angular position for maximum SHG indeed occurs at $\Phi = \pi/2$. The result is shown in Fig. 5.7 with a p-in/p-out polarization combination.

Table 5.1. Dichroic ratio D of infrared absorption peaks and angular shift $\Delta\Phi$ of azimuthal patterns with a steady dc field of opposite polarity.

Peak/cm^{-1}	D(–5 V)	D(+5 V)	$\Delta\Phi$/°
1169	5.77	7.30	27
1250	5.39	6.11	26
1439	9.15	9.27	27
1516	7.70	8.08	26
1608	11.30	13.99	27
1763	0.22	0.21	24
2851	0.60	0.57	22
2924	0.39	0.39	21

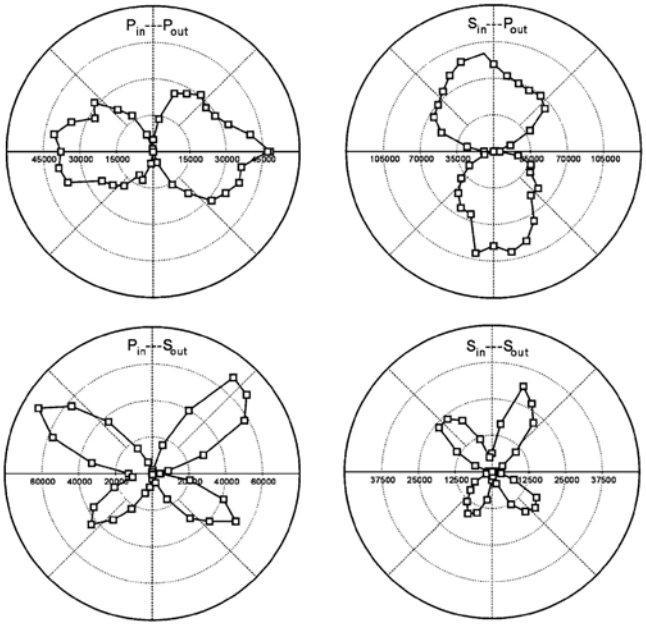

FIG. 5.6. Azimuthal patterns of the second harmonic generation signal from an SSFLC with various polarization combinations. The X-axis (the rubbing direction) of the SSFLC cell is oriented to align with $\Phi = 0$.

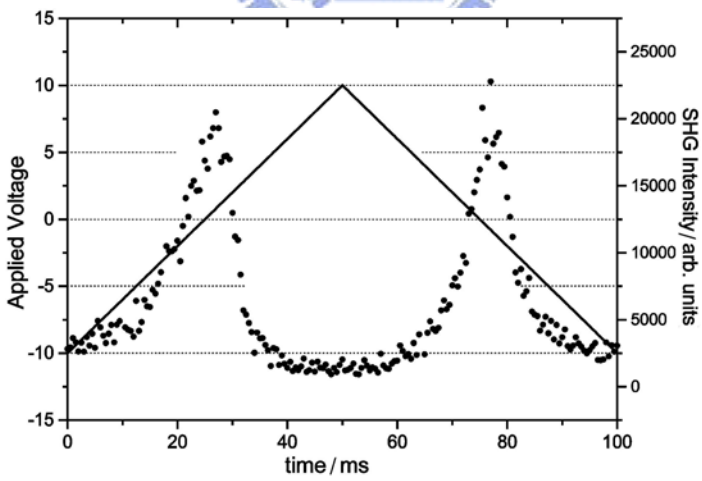

FIG. 5.7. The p-polarized second harmonic signal (filled dots) from an SSFLC cell excited by a p-polarized fundamental beam. The SSFLC cell is driven by a triangular wave form shown by the solid line.

5.3.2. Field-Induced Reorientation

We now analyze the time-resolved electro-optical response of the SSFLC cell to yield information about the field-induced reorientation of the FLC mixture. We insert the SSFLC cell into an optical setup involving a crossed polarizer-analyzer and orient the rubbing direction to align with the transmission axis of the input polarizer. Bipolar square-wave pulses are then employed to excite the SSFLC cell. The field-on period with +10 V extends from 0 to 110 μsec, followed by a field-free duration ranging from 110 to 500 μsec. Then a –10 V period extends from 500 to 610 μsec. The time-resolved optical transmission is monitored as a function of azimuthal angle of the SSFLC.

From the results presented in Fig. 5.8, it can be seen that during the field-on period the symmetry axis of the azimuthal pattern rotates rapidly with a reduction of modulation depth. During the field-free period, the orientation of the azimuthal pattern does not change significantly, instead a slow recovery of the modulation depth is observed. A better presentation can be achieved by fitting the measured patterns to $A(\Phi) = b(t) + a(t)\sin^2[\Phi - \omega(t)] + c(t)\sin^2[2\Phi - 2\omega(t)]$. The resulting $a(t)$, $b(t)$, $c(t)$, and $v(t)$ are shown in Fig. 5.9. The time curve of the switching SSFLC director appears to be symmetric in the positively and negatively driven periods. The contrast ratio of the optical transmission decreases during the field-on period, as shown by a rapid increase of the isotropic component $b(t)$. The isotropic component then slowly decreases with an accompanying increase of $a(t)$ and $c(t)$ after the field is switched off. The optical axis of the SSFLC cell can complete a field-induced rotation in 66 μsec.

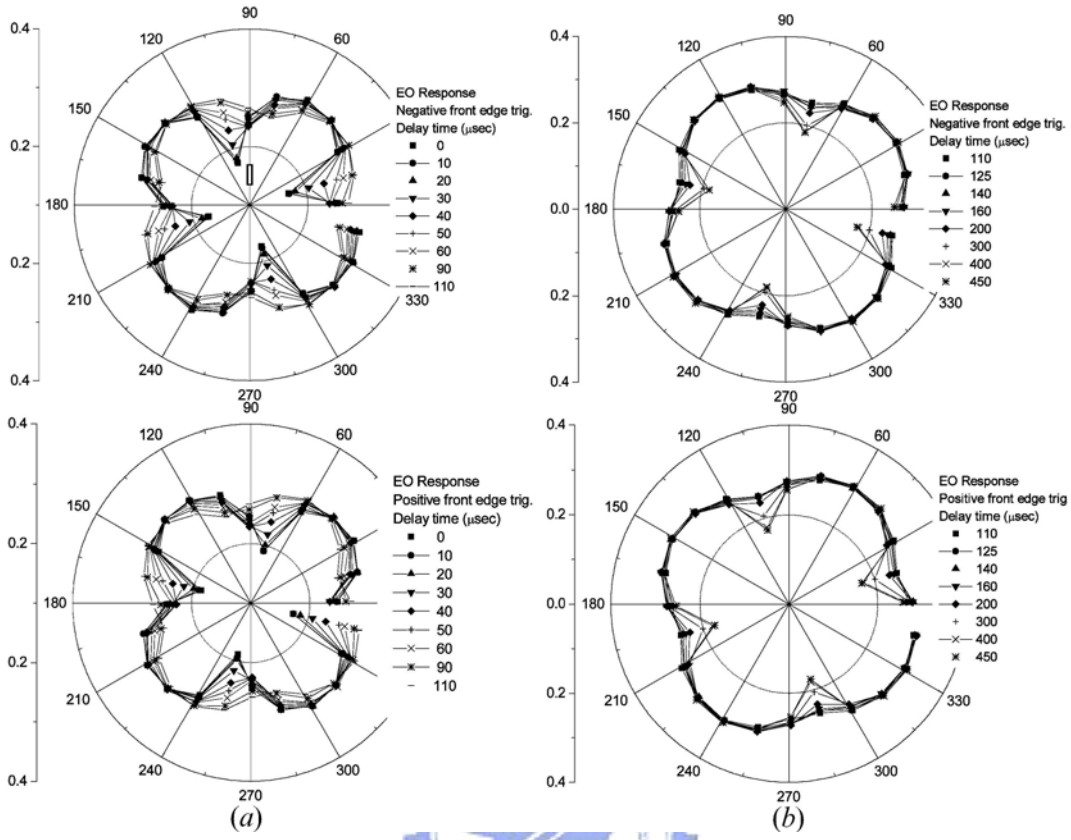

FIG. 5.8. Electro-optical azimuthal patterns measured on an SSFLC during (a) the field-on, and (b) field-free durations. The direction of the incident polarizer is along the 0 degree. A square-wave voltage pulse of duration 110 μsec and amplitude of –10 V (top) and +10 V (bottom) was used.

The optical contrast can change with cell thickness, driving voltage and FLC cone angle. In our case, the cell thickness is close to the half-wave thickness of the FLC mixture. The cone angle of our SSFLC (28°) is about 5° away from the desired 22.5°. Therefore the optical contrast of the SSFLC cell is not in the optimum condition. However, based on the dichroic ratio of IR absorption peaks listed in the Table 5.1, we can conclude that the alignment quality of the SSFLC cell is either similar or even better than results shown in the literature.[84]

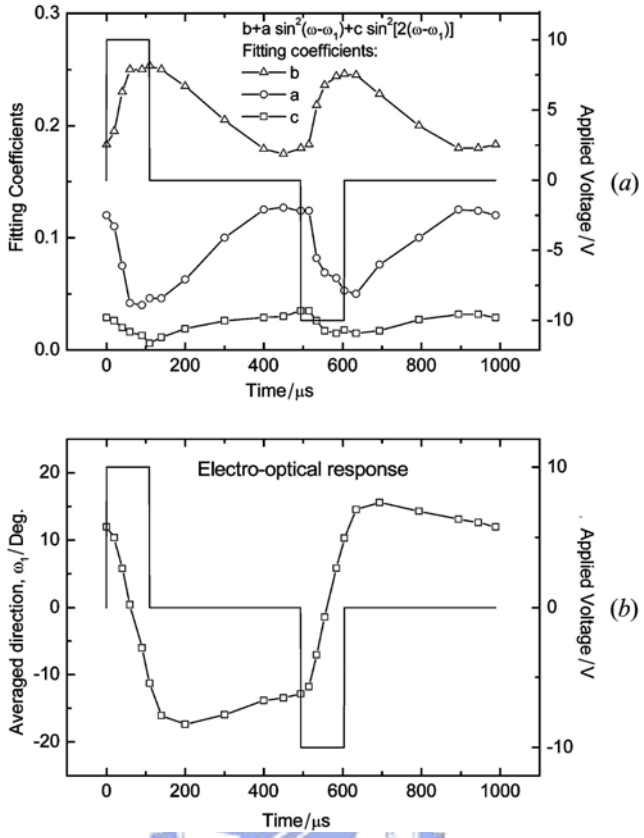

FIG. 5.9. (a)Fitting parameters (symbols) of the electro-optical azimuthal patterns and the applied voltage (solid line) are plotted as a function of time. (b) The deduced orientation angle of the optic axis of FLC film is shown as open squares. Rubbing direction of the FLC cell is along the 0°.

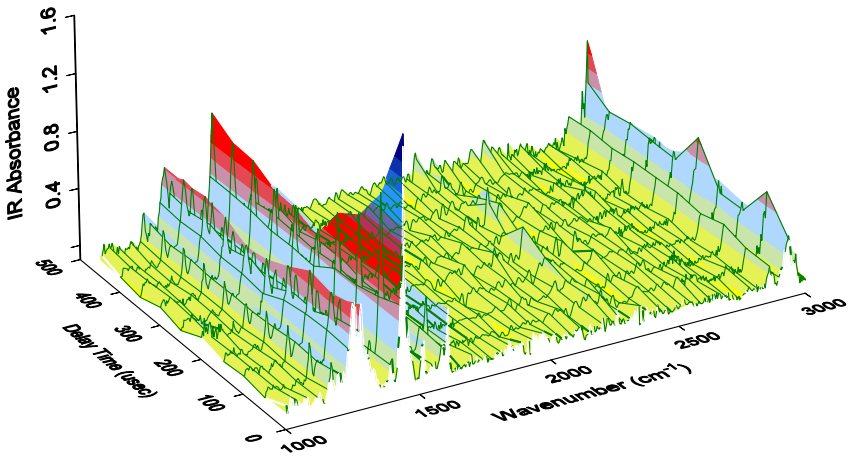

FIG. 5.10. Time-resolved FTIR spectra taken from an SSFLC, which is excited by +10 V pulse extending from 0 to 110 μsec.

The switching dynamics can be better understood by monitoring the field-induced reorientation of different molecular segments with trFTIR. The results with an SSFLC excited by +10 V from 0 to 110 μsec are shown in Fig. 5.10.

We note that the orientation distribution of molecular segments with an applied dc voltage is narrower than for an SSFLC driven by a pulsed electric field. This reflects the fact that contrast ratio with a dc voltage is better than in the switching process. The FTIR azimuthal patterns of groups of atom associated with the FLC core reorient, and the resulting angular orientation $\omega(t)$ is shown in Fig. 5.11. All the groups of atoms selected are found to follow an almost identical field-on time course of field-induced reorientation. This indicates that the LC cores in the FLC mixture behave somewhat as a rigid unit during the field-on period. However, when the applied field is switched off, all core segments immediately reverse their rotating direction. Then they relax from ϕ ~180° to the steady-state orientation (ϕ ~120°) with slightly different speeds. This suggests that the core segments in the FLC mixture do not behave as a rigid unit in the field-free condition. Apparently, intermolecular interaction among homologous species is not strong enough to forbid different relaxation pathways of the core segments. This behavior does was not observed in the EO measurement. Moreover, unlike the symmetric behavior in the EO response, our trFTIR study also reveals that the switching process of the core segments in the positively driven period is different from that driven by a negative pulse. The asymmetry might relate to the broken mirror symmetry in the chiral FLC mixture. Supporting data can also be obtained with SHG, as shown in Fig. 5.6, where the p-in/s-out SH azimuthal pattern exhibits asymmetry about the XZ-plane and a non-vanishing s-in/s-out SH activity was observed.

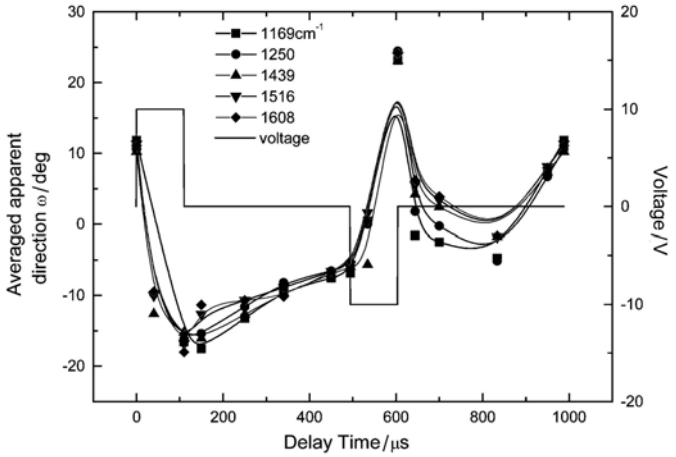

FIG. 5.11. Transient orientations of several atomic segments associated with the FLC cores are presented as a function of delay time. Note that the azimuthal angle can be determined from $\phi(t) = \cos^{-1}[\tan\omega(t)/\tan\theta]$.

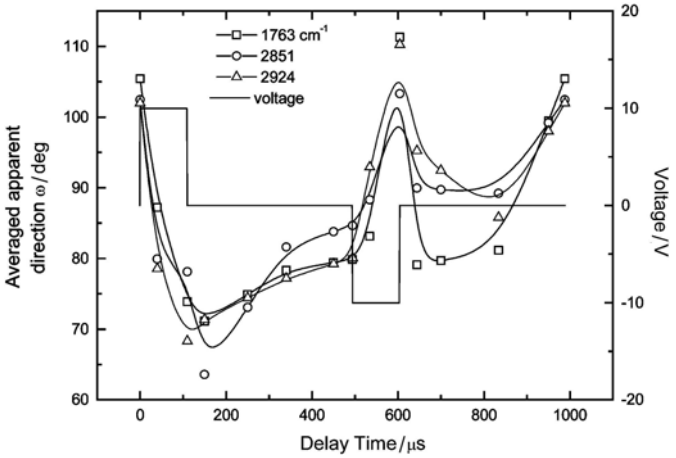

FIG. 5.12. Transient orientations of several atomic segments associated with C=O moiety and alkyl chain are presented as a function of delay time. The solid lines are drawn for eye-guiding only.

For all other groups of atoms not associated with the FLC cores, the time courses of field-induced reorientation are presented in Fig. 5.12. As shown in Fig. 5.2, the IR polarization with maximum absorbance by these IR dipole moments is perpendicular to the FLC director. Except for the 90° difference, the C=O moiety behaves like the core groups shown in Fig. 5.11. For CH_2 on the alkyl chains, a larger deviation from the time course of the core groups was observed, which

reflects the more flexible nature of the alkyl chains during the field-induced reorientation process.

5.4. Summary

We have found from time-resolved electro-optical (EO) measurements that all FLC molecules rotate in unison about the layer normal. Although the rotational motion of the FLC director can respond quickly to the applied field, the molecular orientation distribution is found to spread out at first and then slowly converge to the new direction of the FLC director. The azimuthal patterns of FTIR absorption lines associated with the FLC core follow the same time course, as shown by the EO measurement with an electric field. When the applied field is switched off, all core segments immediately reverse their rotating direction, and then relax to their steady-state direction with varying relaxation speeds. However, unlike the symmetric behavior observed with the EO measurement technique, the FTIR time-course reveals that the core segments behave differently in a positively driving field from when driven by a negative pulse. A more rapid field-free relaxation was observed for the core groups after the negative driving pulse. Among groups of atoms not associated with FLC cores, the C=O moiety behaves like those core groups, while CH_2 groups on the alkyl chains are more flexible during the field-induced reorientation process. We conclude that submolecular fragments of different molecular species in the FLC mixture can move correlatively in a steady dc field and during the field-induced re-orientation process.

Chapter 6

2D IR Correlation Spectroscopy of a Neat Surface Stabilized Ferroelectric Liquid Crystal

Owing to the advantages of fast response, bistability and wide viewing angle, ferroelectric liquid crystal (FLC) has become a promising material for the next generation display.[3,76] For the interests of both fundamental research and industrial applications, many efforts have been made to investigate the molecular deformation and the switching behavior of FLC materials.[74,78,79] Polarized Fourier transform infrared (FTIR) absorption spectroscopy and time-resolved IR spectroscopy had been used to probe molecular conformation in a ferroelectric liquid crystal during the large-scale collective reorientation induced by the an external electric field.[22,23,25,26,80,87] One of the most controversial issues in this kind of studies is whether the electrical field-induced reorientation of FLC molecules is rigid or flexible. The answer could be obtained with the study of a neat FLC material.

Two dimensional (2D) correlation spectroscopy is a technique where the spectral intensity is plotted as a function of two independent spectral variables.[60] By spreading peaks along the second spectral dimension; one can gain advantage to sort out complex or overlapped spectral features that normally cannot be detected along the first spectral dimension. Owing to the enhancement of spectral resolution and sensitivity of perturbation-induced spectral variation, the 2D correlation analysis has been introduced into the IR spectroscopic studies of the

FLC material.[88-91] However, most studies focus on steady states with single perturbation parameter such as the temperature or the IR polarization angle, and the results are only illustrated qualitatively.

In the following study, a home-built multichannel time-resolved polarized FTIR (trPFTIR) system is employed to investigate the molecular conformational and orientational variations of a surface-stabilized FLC (SSFLC). By using 2D correlation analysis of trPFTIR, interesting results regarding about the electric field-induced switching process of an SSFLC are obtained. The material studied in this chapter is a neat FLC material. This chapter is organized as follows: Sec. 6.1 offers the experimental details. Some theoretical simulations of the 2D IR correlation spectroscopy are depicted in Sec. 6.2. Section 6.3 presents the discussion of the experimental results.

6.1. Experimental Procedures

The SSFLC cells used consist of two CaF_2 plates coated with indium tin oxide (ITO) conducting films and polyimide alignment layers rubbed unidirectionally. The substrates were assembled in a homogeneous geometry with 1.5 μm cell thickness to form a surface stabilized structure. The pretilt angle is controlled to be about 2°. A ferroelectric liquid crystal (S)-(-)-1-cyano-2- methylpropyl 4-(4'-(5-hexenyloxy) biphenyl-4- carbonyloxy) benzoate (CMHCB; Fig. 6.1) was filled into a test cell at a temperature above the isotropic phase. The test cells were then slowly cooled to 108 °C to result in SmC* phase.

Time-resolved FTIR spectra from 900 to 3500 cm^{-1} with 4 cm^{-1} resolution were recorded with a commercial continuous-scan FTIR spectrometer equipped with a liquid nitrogen-cooled HgCdTe detector and home-made data acquisition electronics. Bipolar square-wave pulses were used to excite the SSFLC cell. The waveform includes a +15 V field-on duration extending from 0 to 140 μsec, followed by a field-free period from 140 to 500 μsec. Then a –15 V duration

extends from 500 to 640 μsec, followed by a field-free period from 640 to 1000 μsec. For each polarization angle of the incident infrared beam, a total of 32 time-resolved interferograms were collected.[25] The synchronous and asynchronous 2D correlation analysis with different infrared polarization angles were calculated based upon an algorithm developed by Noda,[60] which was implemented in software named 2Dshige composed by S. Morita.[92]

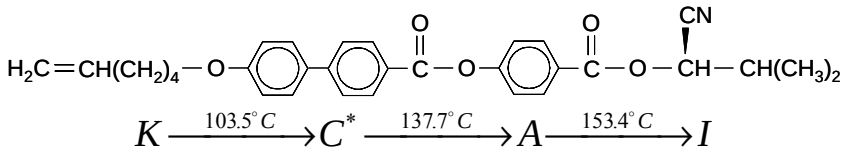

FIG. 6.1. Structure of CMHCB and the phase transition temperature.

6.2. Theoretical Considerations

6.2.1 Absorbance Profiles of Polarized IR Spectra

To describe the arrangement of a molecular fragment, two important parameters of molecular orientation and alignment are generally introduced. These two parameters can be deduced from the absorbance profile $A_p(\Phi)$ which can be obtained from the polarized IR spectra. For normal incidence on the cell substrate, the integrated infrared absorbance by an atomic group *p* can be expressed as[83]

$$A_p(\Phi) = A_{p,0} + U_p \cdot \sin^2(\Phi - \Phi_{p,0}) \tag{6.1}$$

where $A_{p,0}$ and U_p denote the isotropic, and the uniaxial component of atomic group *p* in the film, respectively; and Φ is the angle between the incident infrared polarization E_{IR} and the laboratory x-axis (i.e., the rubbing direction on the cell substrate). The parameter $\Phi_{p,0}$ represents the fragmental orientation. A dichroic ratio DR of the angular pattern $A_p(\Phi)$ can be defined as $DR = (U_p + A_{p,0})/A_{p,0}$. The dichroic ratio, which reflects the degree of uniaxial alignment in an anisotropic

film, is decreased with increasing isotropic component $A_{p,0}$.

6.2.2 Theory of 2D IR Correlation

Two dimensional (2D) correlation spectroscopy is a technique where the spectral intensity is plotted as a function of two independent spectral variables.[60] By spreading peaks along the second spectral dimension; one can gain advantage to sort out complex or overlapped spectral features that normally cannot be detected along the first spectral dimension.

To construct generalized 2D correlation spectra, we shall first calculate a set of dynamic spectra[83]

$$\tilde{I}(\nu;\Phi,t)=\begin{cases} I(\nu;\Phi,t)-\bar{I}(\nu,t) & 0\le\Phi\le 2\pi \\ 0 & \text{otherwise} \end{cases} \tag{6.2}$$

Here $I(\nu;\Phi,t)$ denotes a set of infrared absorption spectra, measured with infrared polarization angle Φ, and t denotes the perturbing parameter, which can be time or temperature. The reference spectrum $\bar{I}(\nu,t)$ is conveniently defined as

$$\bar{I}(\nu,t)=\frac{1}{2\pi}\int_0^{2\pi} I(\nu;\Phi,t)d\Phi \tag{6.3}$$

We can generate two kinds of 2D correlation spectra, known as synchronous $Syn(\nu_1,t_1;\nu_2,t_2)$ and asynchronous $Asyn(\nu_1,t_1;\nu_2,t_2)$ spectra, from the set of dynamic spectra

$$\begin{aligned} C(\nu_1,t_1;\nu_2,t_2) &= \langle \tilde{I}(\nu_1;\Phi,t_1)\tilde{I}(\nu_2;\Phi,t_2)\rangle_{0\le\Phi\le 2\pi} \\ &= Syn(\nu_1,t_1;\nu_2,t_2)+iAsyn(\nu_1,t_1;\nu_2,t_2) \end{aligned} \tag{6.4}$$

The correlation operation <…>$_\Phi$ in Eq. (6.4) is defined as

$$\langle \tilde{I}(\nu_1;\Phi,t_1)\tilde{I}(\nu_2;\Phi,t_2)\rangle_{0\le\Phi\le 2\pi}=\frac{1}{2\pi}\int_0^{2\pi}\tilde{I}(\nu_1;\omega,t_1)\tilde{I}^*(\nu_2;\omega,t_2)d\omega \quad \text{with}$$
$$\tilde{I}(\nu;\omega,t)=\int_0^{2\pi}\tilde{I}(\nu;\Phi,t)\,e^{-i\omega\Phi}d\Phi \tag{6.5}$$

Eq. (6.4) provides a functional comparison of intensity variation $\tilde{I}(\nu;\Phi,t)$ at different spectral variables ν_1 and ν_2 within a fixed interval of the perturbing

variable $0 \le \Phi \le 2\pi$.

6.2.3 Determination of Molecular Configuration with 2D Correlation Analysis

The synchronous and asynchronous correlation spectra directly correspond to the alignment and orientation of the monitored atomic groups, therefore can be utilized to determine the arrangements of molecular fragments. For a set of infrared absorption spectra $I(\nu;\Phi,t)$ measured with infrared polarization angle Φ, and parameter *t*, which can be the time or temperature. The 2D correlation analysis can be performed on the spectra at the same *t* to yield synchronous $Syn_t(\nu_1,\nu_2)$ and asynchronous $Asyn_t(\nu_1,\nu_2)$ correlation, or on the spectra at t_1 and t_2 to yield hetero synchronous correlation $Syn(\nu_1,t_1;\nu_2,t_2)$ and hetero asynchronous correlation $Asyn(\nu_1,t_1;\nu_2,t_2)$, respectively. The relations between the synchronous/asynchronous correlation peaks and the fragment alignment/ orientation are discussed as following.

6.2.3.1 Analyzing the Spectra at the Same t

A. The influence of the isotropic term A_0 on 2D IR correlation

To know whether the isotropic component of an isotropic film affects the auto- and cross-peaks of 2D synchronous correlation spectrum, the polarization angle-dependent pattern of an infrared absorption peak is described by Eq. (6.1) with U = 1 and Φ_0 = 0. We increase A_0 from 0 to 1.5. The resulting polarization-dependent patterns are depicted in Fig. 6.2(a). Figure 6.2(b) presents the calculated intensities of the synchronous auto-peak $Syn_t(\nu_1,\nu_1)$ and cross-peak $Syn_t(\nu_1,\nu_2)$. The result clearly shows that the synchronous auto peak and cross peak are essentially independent of A_0.

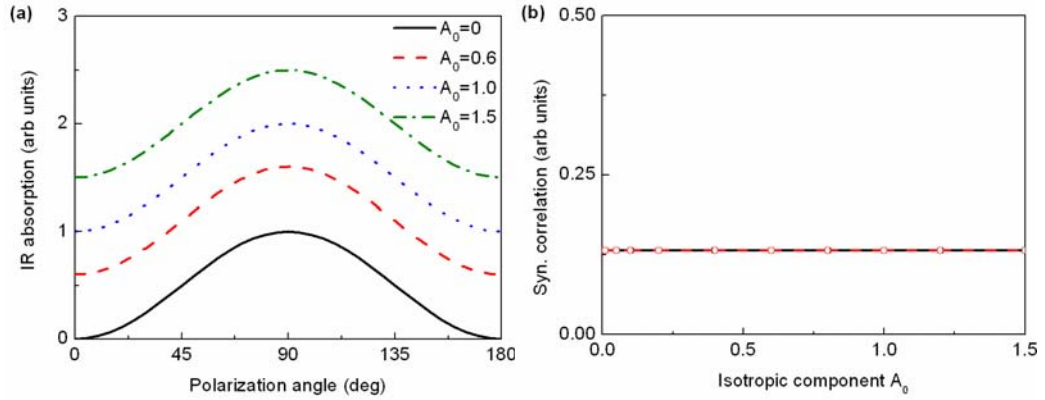

FIG. 6.2. (a) Polarization angle-dependent patterns of infrared absorption peaks are plotted as a function of Φ by fixing U = 1 and Φ_0 = 0 while varying isotropic component A_0 from 0 to 1.5; (b) the corresponding calculated intensities of the synchronous auto-peak $Syn_t(\nu_1,\nu_1)$ and cross-peak $Syn_t(\nu_1,\nu_2)$ as a function of A_0.

B. The influence of the uniaxial component *U* on 2D IR correlation

To find out how the parameter U affects the synchronous correlation spectra, we assume the polarization-dependent pattern of infrared absorbance to have $A_0 = 0.1$ and $\Phi_0 = 0$. Then we increase U from 0.05 to 2.5 to simulate the correlation spectra. The resulting polarization-dependent patterns are depicted in Fig. 6.3(a). Figure 6.3(b) presents the calculated $Syn_t(\nu_1,\nu_1)$ and $Syn_t(\nu_1,\nu_2)$ of the 2D synchronous correlation. We found in Fig. 6.3(b) that the two correlation signals monotonically increase with U but in a different function form. The simulation results show that for the synchronous auto-peak, the intensity variation with U can be properly described by $Syn_t(\nu_1,\nu_1) = 0.1318U(\nu_1)^2$, while for the synchronous cross-peak, it becomes $Syn_t(\nu_1,\nu_2) = 0.1318U(\nu_1)U(\nu_2)$. Therefore, by referring to a specific $U(\nu_1)$, $Syn_t(\nu_1,\nu_2)$ becomes a linear function of $U(\nu_2)$. This provides a method to deduce the degree of uniaxial alignment U from the synchronous cross-peak height.

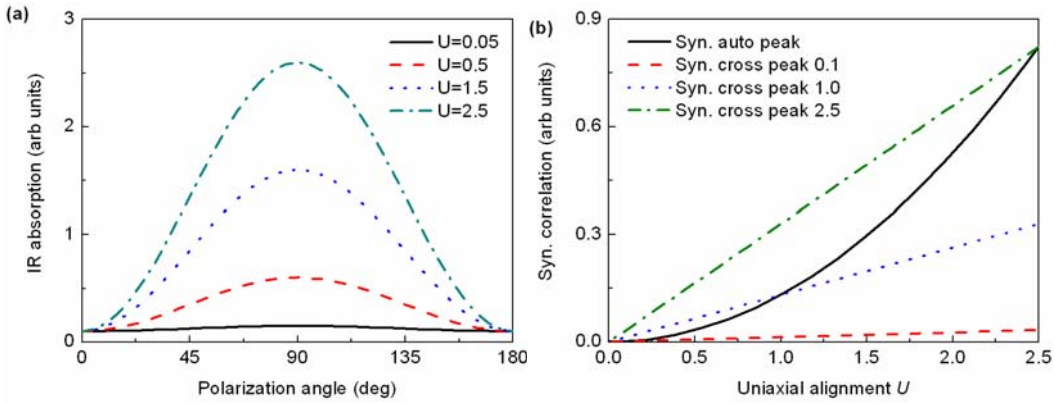

FIG. 6.3. (a) Polarization angle-dependent patterns of infrared absorption peaks are plotted as a function of Φ by fixing A_0 at 0.1 and $\Phi_0 = 0$ while varying uniaxial alignment parameter U from 0.1 to 2.5; (b) the calculated intensities of the synchronous auto-peak $Syn_t(\nu_1,\nu_1)$ (solid curve) as a function of $U(\nu_1)$ and the cross-peaks $Syn_t(\nu_1,\nu_2)$ as a function of $U(\nu_2)$ by fixing $U(\nu_1)$ to 0.1 (long dashed), 1.0 (dotted), and 2.5 (dashed dotted curve).

C. The influence of the orientation Φ_0 of molecular fragment

To explore the influences from the fragment orientation, we assume the IR absorbance profile to have $A_0 = 0.1$ and $U = 1$, and vary Φ_0 from 0° to 90° to calculate the correlation curves. The resulting polarization-dependent patterns are presented in Fig. 6.4(a). Figure 6.4(b) depicts the calculated intensities of the synchronous auto-peak $Syn_t(\nu_1,\nu_1)$ and the cross-peak $Syn_t(\nu_1,\nu_2)$. The synchronous auto-peak height varies with Φ_0 by $Syn_t(\nu_1,\nu_1) = 0.1318 - 0.0066\sin^2[2\Phi_0(\nu_1)]$. Owing to the small prefactor of sinusoidal function, $Syn_t(\nu_1,\nu_1)$ is insensitive to Φ_0. But for the synchronous cross-peak (see the dashed curve of Fig. 6.4(b)), which can be expressed as $Syn_t(\nu_1,\nu_2) = 0.1318\cos[2(\Phi_0(\nu_1) - \Phi_0(\nu_2))]$, it can vary sensitively with Φ_0. From the simulation, the asynchronous correlation is found to depend only on the orientation and the auto-peak heights are always zero. In addition, the asynchronous cross-peak can be properly described with $Asyn_t(\nu_1,\nu_2) = 0.11\sin[2(\Phi_0(\nu_1) - \Phi_0(\nu_2))]$ (Fig. 6.4(c)), which is also useful to reflect the orientational variation of molecular fragments in a complex material.

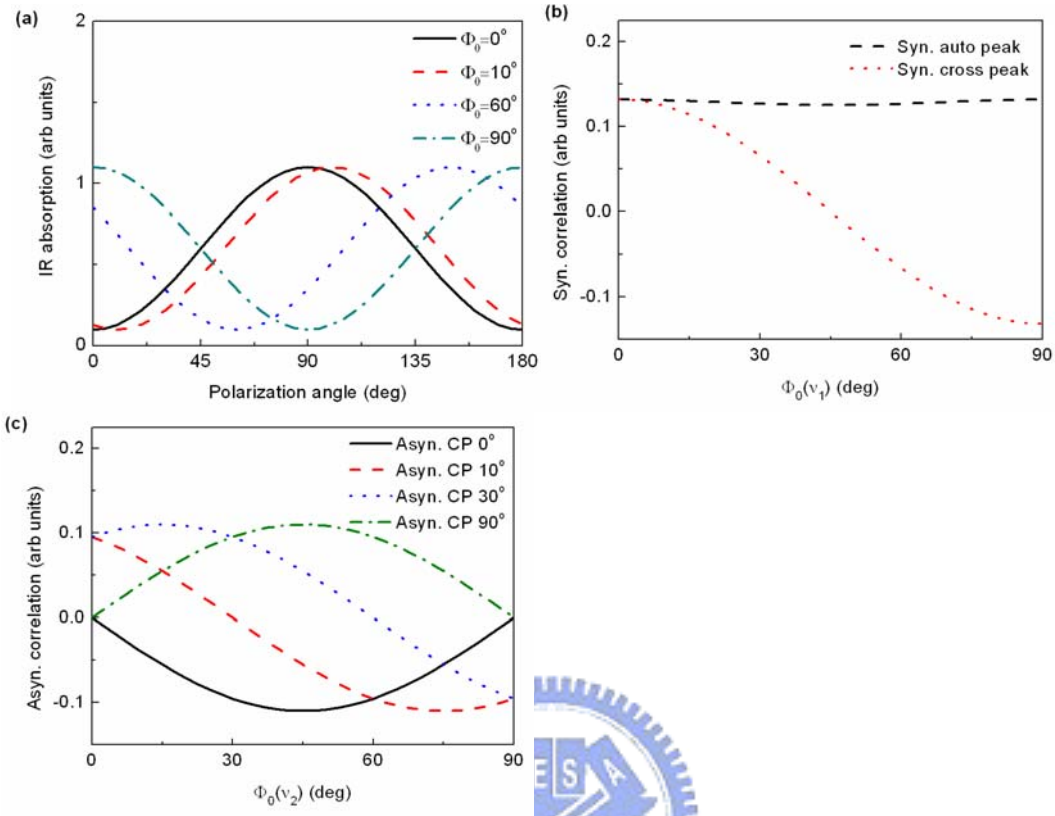

FIG. 6.4. (a) Polarization angle-dependent patterns of infrared absorption peaks are plotted as a function of Φ by fixing A_0 at 0.1, U = 1.0 while varying Φ_0 from 0° to 90°; (b) the calculated intensities of the synchronous auto-peak $Syn_t(\nu_1,\nu_1)$ (dashed curve) and the cross-peaks $Syn_t(\nu_1,\nu_2)$ (dotted curve) as a function of Φ_0 ; (c) the calculated intensities of the asynchronous cross-peak $Asyn_t(\nu_1,\nu_2)$ as a function of $\Phi_0(\nu_2)$ by varying $\Phi_0(\nu_1)$ from 0° to 90°.

6.2.3.2 Analyzing the Spectra at Different t

In the case of analyzing the spectra at different *t*, the alignment variation of fragments induced by parameter *t* can be revealed. In the synchronous hetero correlation spectra, the auto-peak $Syn(\nu_1,t_1;\nu_1,t_2)$ of a specific mode at ν_1 can be influenced by the degree of uniaxial alignment *U* and the orientation angle Φ_0. However, the hetero asynchronous auto-peak height varies only with the fragment orientation Φ_0 by $Asyn(\nu_1,t_1;\nu_1,t_2)=0.11\sin[2(\Phi_0(\nu_1,t_1)-\Phi_0(\nu_1,t_2))]$. Therefore for a specific functional group, we can use $Asyn(\nu_1,t_1;\nu_1,t_2)$ to reflect the

orientation changes between t_1 and t_2.

The above discussion shows that the synchronous auto-peaks can be influenced by the uniaxial parameter U of the molecular fragments, while only the variation of Φ_0 induced by parameter t can alter the hetero asynchronous peak heights. Therefore by combining these two pieces of information together, the correlated motions of molecular fragments in the FLC material can be resolved unambiguously.

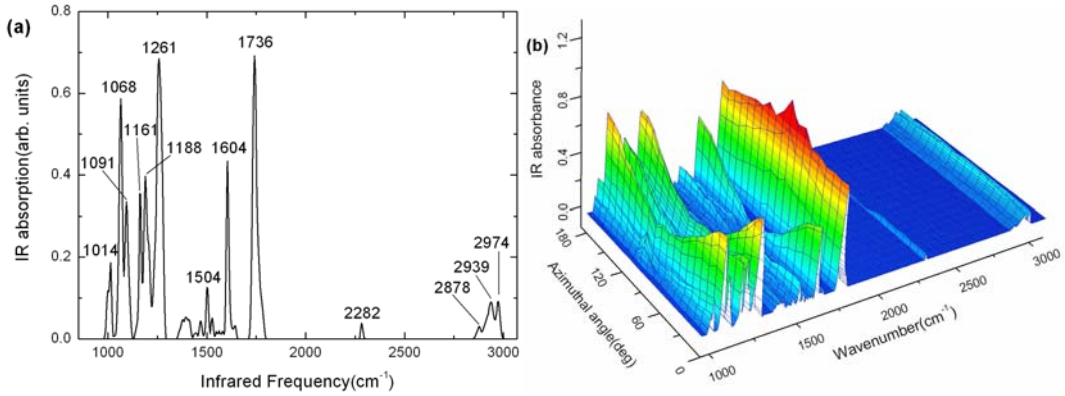

FIG. 6.5. (a) Infrared absorption spectrum of an SSFLC cell of CMHCB in SmC* at 108 °C; (b) A set of polarized IR spectra for the SSFLC cell at 108 °C and zero field for a number of polarizer rotation angles Φ in the range 0°–180°.

6.3. Results and Discussion

6.3.1 Assignment of Infrared Absorption Bands

Figure 6.5(a) presents an infrared absorption spectrum of CMHCB. The IR spectral peaks at 1068, 1091, 1161, 1188, 1261, 1504, 1604, 1736, and 2282 cm^{-1} can be attributed to the normal modes associated with the cores; and the peaks at 2939 and 2974 cm^{-1} to the alkyl chains.[83] The peaks at 2974 and 2878 cm^{-1} are noted to originate from the anti-symmetric and symmetric CH_3 stretching mode, whereas the peak at 2939 cm^{-1} are from the anti-symmetric CH_2 stretching along the alkyl chains. The peak at 1736 cm^{-1} is believed to be from the C=O stretching modes. The peaks at 1604 and 1504 cm^{-1} are mainly from the C=C stretching modes of the

benzene ring. The normal modes at 1068, 1091, 1188, and 1261 cm^{-1} are associated with the C–O–C stretching modes. The remaining mode at 1161 cm^{-1} is attributed to the CH stretching modes. We can see in Fig. 6.5(b) that spectral peaks associated with the cores exhibit an opposite angular dependence on the infrared polarization with that associated with carbonyl group. The peaks contributed from the alkyl chains show only slight angular dependence. Similar result had also been observed on other FLC materials.[84]

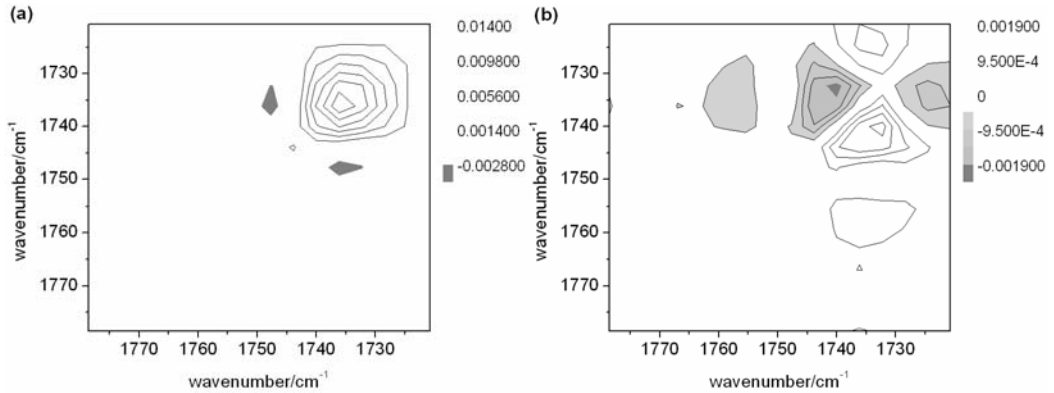

FIG. 6.6. (a) Synchronous 2D IR correlation plot in the 1720–1780 cm^{-1} region generated from the polarization-angle dependent spectra of CMHCB at 108 °C in the field-free virgin state, (b) the corresponding 2D IR asynchronous correlation plots.

Owing to the abilities to decouple the overlapped peaked and to distinguish functional groups attached to different positions in a molecule, we use the 2D IR correlation analysis of the polarization-angle dependent patterns to gain more insight into the correlated motion of the functional groups. Figure 6.6 shows the synchronous (a) and asynchronous (b) correlation plots in the 1720–1780 cm^{-1} region, obtained from an SSFLC cell in a field-free virgin state. The synchronous correlation plot exhibits one strong auto peak at 1736 cm^{-1} (also shown in Fig. 6.5) which is corresponding to the stretching mode of carbonyl group. However, two cross peaks at 1732 and 1740 cm^{-1} were observed in the asynchronous correlation plot. The modes at 1732 cm^{-1} are mainly attributed to from the carbonyl groups near the chiral center and the modes at 1740 cm^{-1} are from the molecular core part.

The splitting band at 1736 cm^{-1} strongly suggests that the orientational information of the molecular fragments can be revealed with the 2D correlation analysis, even that their IR spectral peaks are not distinguishable.

6.3.2 Polarized FTIR Spectra in the K Phase and SmC* Phase

The determination of the molecular arrangement in the various phases of an SSFLC cell is important for the understanding of the changes of molecular conformation and distribution in different phases. The polarized FTIR spectra of CMHCB in the K phase (at 65 °C) and SmC* phase (at 108 °C) were measured in field-free condition. Some major peaks are selected to analyze the azimuthal absorbance profiles in these two phases. To investigate the correlated variations of the functional groups, the 2D correlation analysis is performed on the resulting polarized spectra. The relative orientational changes of specific molecular fragments between the K and SmC* phases are studied with the 2D hetero correlation analysis.

To probe the conformation and orientational changes of the CMHCB molecular fragments caused by the phase transition, the absorbance profiles of selected bands were deduced from the polarized IR spectra. Figure 6.7 shows the azimuthal patterns of peak absorbance measured at 65 °C (K phase) and 108 °C (SmC* phase), where the 0 degree is along the rubbing direction. The dot symbols represent the experimental data and solid curve is the fitting curves to Eq. (6.1). Comparing the azimuthal absorbance patterns of 1604 and 1261 cm^{-1} at 65 °C and those at 108 °C (Figs. 6.7(a) and 6.7(b)), the maximum absorbance intensities are larger in the SmC* phase than that in the K phase, but the minimum absorbance intensities almost keep constant in these two phases. Since both the 1604 and 1261 cm^{-1} correspond to the molecular core part, the maximum absorbance increase in the SmC* phase could be attributed to the phase-induced reorientation of the molecular core part. The minimum absorbances at 1604 and 1261 cm^{-1} are nearly equal in the K and SmC*, suggests that the distribution width of the molecular core

is preserved during the phase transition. The azimuthal absorbance patterns of 2974 cm^{-1} in the K and SmC* phases (see Fig. 6.7(c)) are almost the same, indicating that the orientational distribution of alkyl chains are isotropic and therefore insensitive to the phase change. However, the absorbance azimuthal pattern of the 1161 cm^{-1} peak shown in Fig. 6.7(d) exhibits smaller maximum and minimum absorbance, but a larger dichroic ratio at 65 °C, suggesting that the phase-induced distribution change of the CH groups is different from that of the molecular core part.

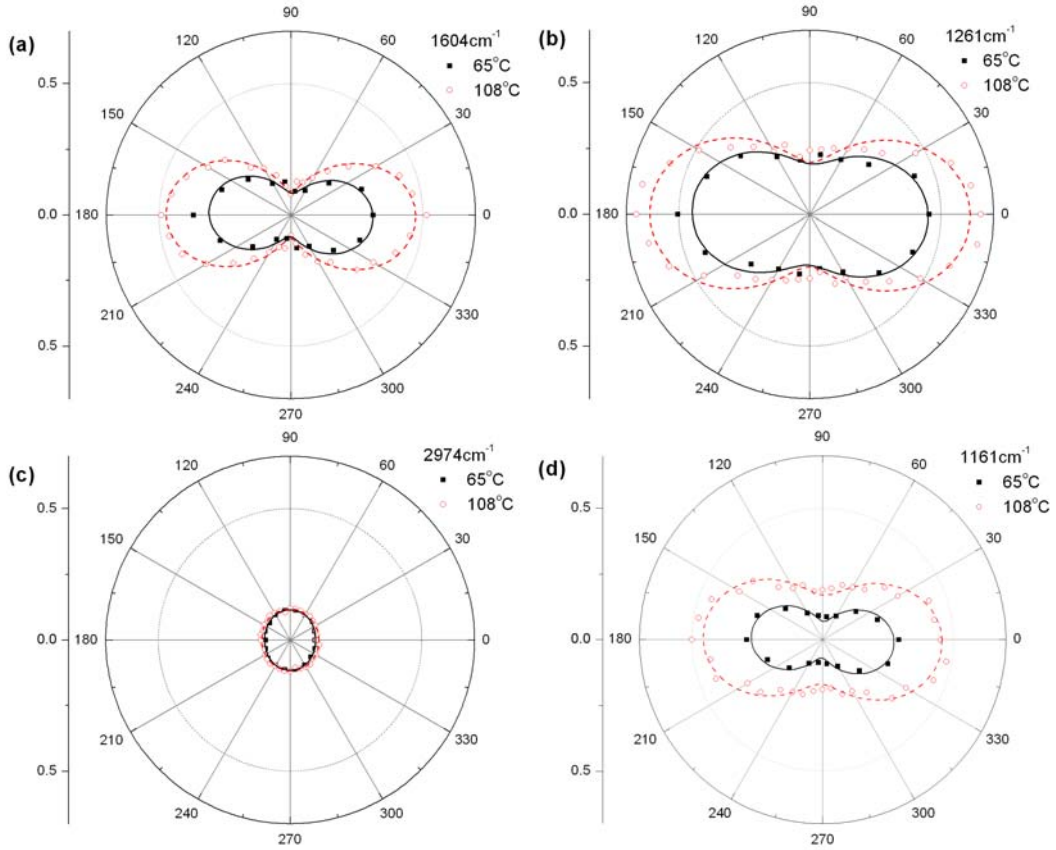

FIG. 6.7. The azimuthal absorbance profiles of IR peaks at (a) 1604, (b) 1261, (c) 2974 and (d) 1161 cm^{-1} at 65 °C (solid symbols) and 108 °C (open symbols) in the field-free virgin state. The lines are the fitting curves.

The main difference between the SmC* and K phases is that, unlike in the liquid crystal phase, the molecules in the crystalline phase are more ordered with a periodic structure and have no liquidity. The molecular orientations in these two

phases are schematically presented in Fig. 6.8. The molecular alignments in the SmC* phase exhibit the orientational order and the layer structure, but lack for the in-layer and inter-layer positional orders. However, the molecules in the K phase possess long-range positional order in three dimensions, in which the interlayer packing is also correlated over long distances, producing a crystalline structure. According to the azimuthal absorbance patterns shown in Figs. 6.7(a) and 6.7(b), the maximum absorbances of the core fragments in the two phases can be found in the same azimuthal angle, suggesting that the FLC molecular core shall be tilted with respect to the layer normal in the K phase. Therefore the tilting angle Θ of molecular core becomes larger in the K phase, resulting in the smaller maximum absorbances compared to those in the SmC* phase.

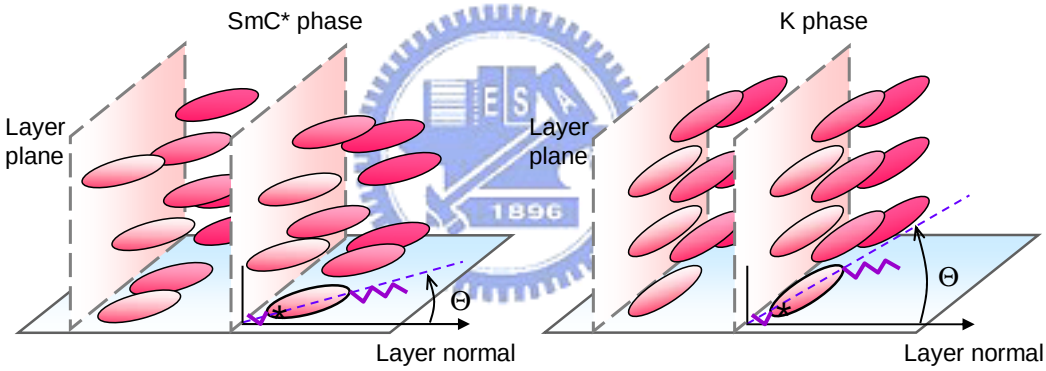

FIG. 6.8. The schematic illustration of the molecular orientations in the SmC* and K phases. Θ is the tilting angle of the molecular core with respect to the layer normal.

The 2D synchronous correlation spectra in the 1490–1640 cm^{-1} region at 65 °C and 108 °C are presented in Figs. 6.9 (a) and 6.9(b), which are generated from an SSFLC cell in a field-free virgin state. Two main auto-peaks locate at 1504 and 1604 cm^{-1}, which correspond to the C=C stretching modes of the benzene rings, were found in both figures. These peaks also exhibit distinctive cross peaks, indicating significant correlation existing between these modes. We also found that the auto peak heights at 108 °C are significantly larger than those at 65 °C. Similar behavior can also be observed in the auto peaks at 1261 and 1188 cm^{-1} (not shown

here). These results indicate that the C=C bonds and C–O–C bonds in the molecular core exhibit a higher degree of uniaxial alignment in the SmC* phase than that in the K phase, which is consistent with the observations from the azimuthal absorbance profiles shown in Figs. 6.7(a) and 6.7(b).

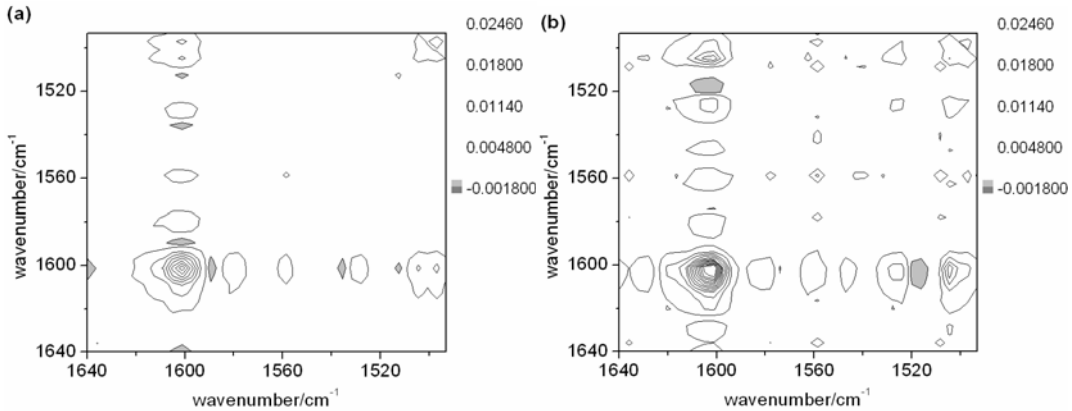

FIG. 6.9. Synchronous 2D IR correlation plot in the field-free virgin state generated from the polarization-angle dependent spectra of CMHCB in the 1490–1640 cm^{-1} region at (a) 65 °C and (b) 108 °C.

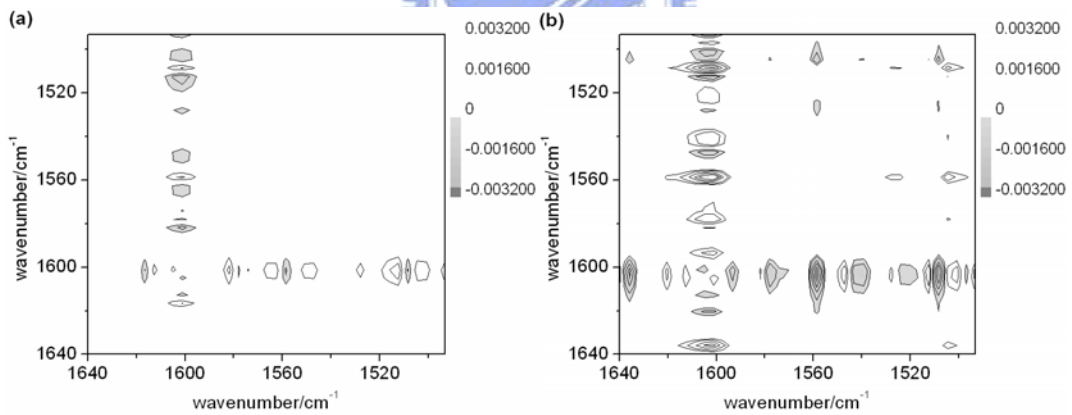

FIG. 6.10. Asynchronous 2D IR correlation plot in the field-free virgin state generated from the polarization-angle dependent spectra of CMHCB in the 1490–1640 cm^{-1} region at (a) 65 °C and (b) 108 °C.

To investigate the angular spreads of molecular fragments in the different phases, the asynchronous 2D correlation plots of the field-free structure in the 1490–1640 cm^{-1} region at 65 °C and 108 °C are shown in Figs. 6.10(a) and 6.10(b). The asynchronous cross peak features are less distinctive at 65 °C, but become distinctive at 108 °C, indicating that significant orientational deviation may exist

among these C=C stretching modes. This result can be understood by noting that in the SmC* phase with unwound structure, the thermal fluctuations of the azimuthal angle ϕ of the director about a tilted cone (Goldstone mode) are allowed.[85,86]

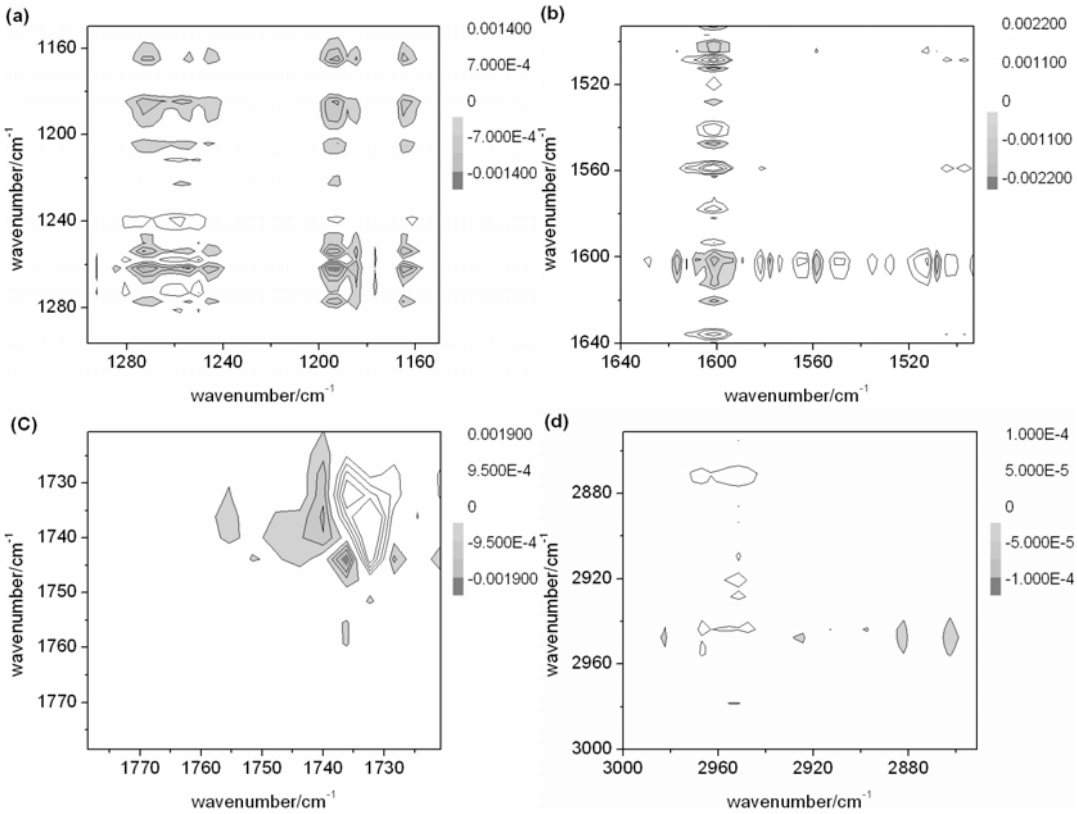

FIG. 6.11. Asynchronous 2D IR hetero correlation plot in the field-free virgin state generated from the polarization-angle dependent spectra of CMHCB between at 65 °C and 108 °C in the (a) 1150–1300, (b) 1490–1640, (c) 1720–1780 and (d) 2850–3000 cm^{-1} regions.

The 2D asynchronous hetero correlation analysis of the polarized-angle dependent spectra in the K phase and SmC* phase can reflect the phase-induced reorientations of molecular segments. The asynchronous hetero correlation plots of CMHCB in the field-free states at 65 °C and 108 °C in the regions of 1150–1300, 1490–1640, 1720–1780 and 2850–3000 cm^{-1} are shown in Figs. 6.11(a)–6.11(d). The absence of auto peak in Fig. 6.11(d) indicates that the fragmental orientations of alkyl chains do not change with the phase transition. This result is similar to that

of Fig. 6.7(c). We noted that the synchronous hetero correlation of 1740 cm^{-1} is negative (not shown here), which means that the distributions of 1740 cm^{-1} at 65 °C and 108 °C are out of phase. Therefore a positive auto peak at 1732 cm^{-1} and a negative one at 1740 cm^{-1} (see Fig. 6.11(c)) shall represent that the chiral carbonyl group and the core C=O reorient along the same directions during the K to SmC* transition. As for the molecular fragments corresponding to the core part, negative auto peaks are identified at 1604, 1261 and 1188 cm^{-1}, but the 1504 cm^{-1} peak is positive (see Figs. 6.11(a) and 6.11(b)). The different signs of the auto peaks suggest that the phase-induced reorientations are not identical for different molecular fragments.

6.3.3 Time-Resolved 2D IR Correlation Analysis

The switching dynamics of CMHCB in SmC* phase can be better understood by monitoring the field-induced reorientation of different molecular segments with trFTIR. Bipolar square-wave pulses are employed to excite the SSFLC cell. The +15 V field-on duration extends from 0 to 140 μsec, followed by a field-free period ranging from 140 to 500 μsec. Then a –15 V duration extends from 500 to 640 μsec, and again followed by a field-free period ranging from 640 to 1000 μsec. Time-resolved infrared absorption spectra were taken as a function of infrared polarization angle. To gain more insight into the correlated motions of the functional groups, the resulting time-resolved polarization angle-dependent patterns of infrared absorption peaks are subject to 2D correlation analysis and the time courses of the synchronous and the hetero asynchronous peaks are deduced.

Figure 6.12(a) presents a comparison of the dichroic ratio (filled symbols) and the synchronous auto peak (open symbols) of the C=C stretching mode at 1604 cm^{-1}, which are associated with the LC core segments. Minor differences between the dichroic ratio and the synchronous auto peak can also be detected. The deviations can be attributed to originate from the isotropic component of the film, which has an effect on the dichroic ratio but can not affect the synchronous auto

peak. The comparison between the apparent angle and the hetero asynchronous auto-peak height is shown in Fig. 6.12(b). An excellent correlation between the apparent angle and the hetero asynchronous auto peak height was observed. The 2D hetero asynchronous auto-peak can therefore be used to monitor the variation of $\Phi_{p,0}$ of a molecular fragment of a complex material. To study the dynamic reorientation processes of molecular fragments, the hetero asynchronous correlation are calculated with the spectra of the field-free state and the transient state at time *t*.

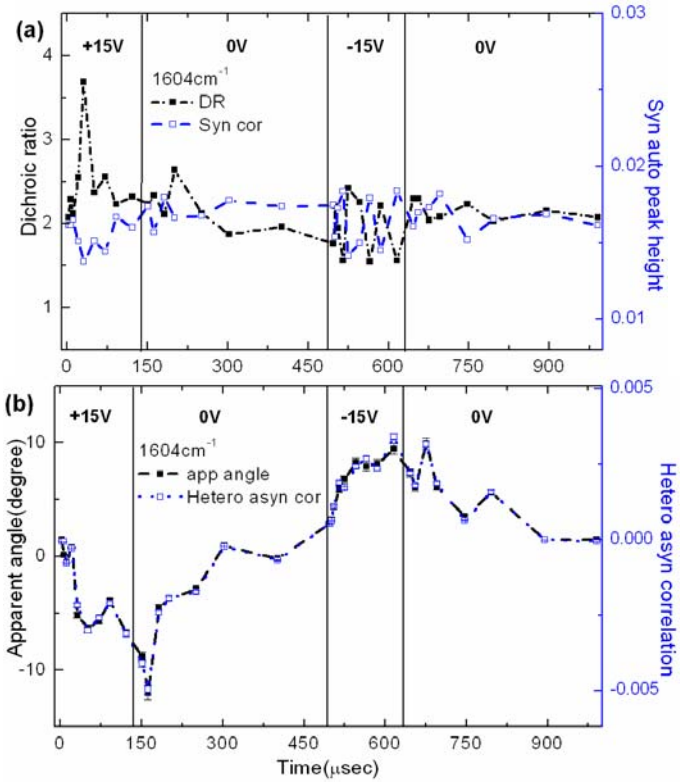

FIG. 6.12. Comparison of (a) the dichroic ratios (filled symbols) and the 2D IR synchronous auto peak (open symbols), and (b) the apparent angles (filled symbols) and the 2D IR hetero asynchronous auto peak (open symbols) of C=C stretching mode at 1604 cm^{-1}.

The dynamic variations of the hetero asynchronous auto peaks of the C=C stretching modes at 1504, 1604 1635, and 1261 cm^{-1} are presented in Fig. 6.13(a). The peaks at 1504 and 1604 cm^{-1} are mainly from the C=C stretching modes of the benzene rings and the 1635 cm^{-1} is from the vinyl group. The peak at 1261 cm^{-1}

comes from the C–O–C stretching modes of the rings. From the time courses of hetero asynchronous peaks, the C=C stretching modes at 1604 cm^{-1} first undergo a rapid orientation change during the field driving cycle, following a slowly relaxation to the direction of the field-free state. Compared to that at 1504 cm^{-1}, the C=C stretching modes at 1604 cm^{-1} exhibits larger hetero asynchronous peak height variation, suggesting that the C=C stretching mode at 1504 cm^{-1} rotates on the cone with a smaller apparent angle during the field-induced switching process. The synchronous (not shown here) and hetero asynchronous peak heights of the vinyl C=C stretching mode at 1635 cm^{-1} are quite small compared to those from the benzene ring. Note that a zero synchronous correlation means that the transient orientational distribution of a molecular segment is isotropic, while a zero asynchronous hetero correlation denotes that at this instant the transient orientation of a molecular segment is along to its field-free virgin direction. Therefore this finding can be attributed to the flexible CH_2 chain which connects the vinyl group to the FLC core which allows the vinyl group to rotate along the molecular long axis with a higher degree of freedom. This could lead to a random distribution and negligible field-induced orientation variation. We also detect field polarity-induced differences in the hetero asynchronous cross peaks. For example, the hetero asynchronous peak height at 1261 cm^{-1} is more distinctive when a negative electric field is applied. The asymmetry with positive and negative fields indicates that the clockwise–anticlockwise symmetry is broken at the level of molecular fragments in CMHCB.

To reveal the switching behavior of the molecular core in detail, the averaged value of hetero asynchronous correlation peak heights is calculated and plotted in Fig. 6.13(b). The two strongest peaks at 1261 and 1604 cm^{-1} are averaged to reflect the core part. This approach is reasonable in view what the optical properties of FLC films are mainly contributed by the molecular core, not by specific stretching modes. During the switching, at the first 40 to 50 μsec after the rising edge of the applying voltage (marked with dotted vertical line in the figure), the time course of

the averaged asynchronous correlation (i.e., the apparent angle of the core) undergoes a rapid change. After the period, the apparent angle changes continuously to an extreme direction than relaxes back to the field-free virgin direction during the field-free periods.

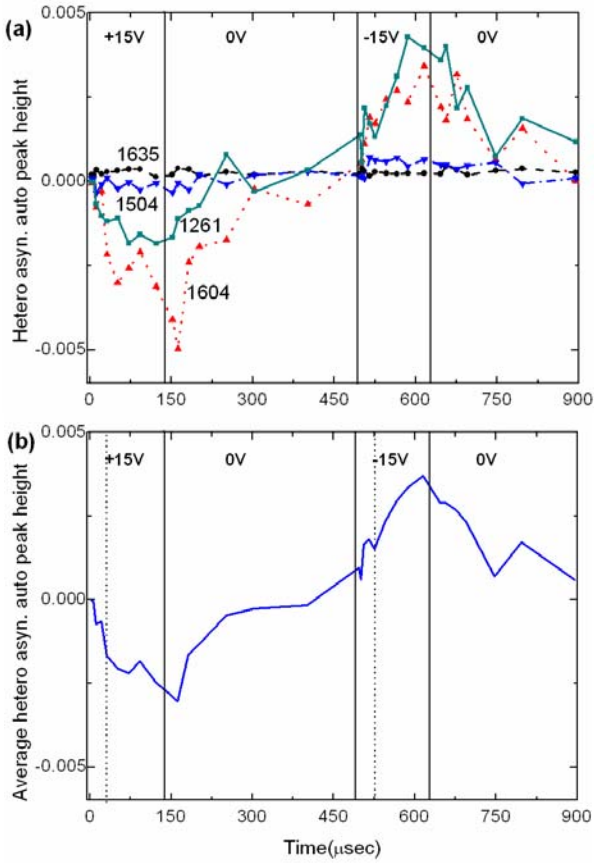

FIG. 6.13. Dynamic variations of (a) the hetero asynchronous correlation of C=C stretching modes and C–O–C stretching modes, (b) the averaged hetero asynchronous correlation of C=C and C–O–C stretching modes.

2D correlation analyses successfully distinguish the C=O groups attached to different locations on a molecule. We can go further to discuss the behaviors of the C=O stretching modes corresponding to the molecular core and the chiral part. The time courses of the synchronous and hetero asynchronous correlation peaks at 1732 (the chiral C=O) and 1740 (the core C=O) cm^{-1} are shown in Figs. 6.14(a) and 6.14(b). The synchronous peak height of the core C=O stretching mode (1740 cm^{-1}) exhibits slightly larger fluctuation compared to the chiral C=O (1732 cm^{-1}) during

the field-free periods, suggesting that the chiral C=O is more restrained than the core C=O. We also noted that the hetero asynchronous correlation peak heights at 1732 and 1740 cm^{-1} show opposite changes from 0 to 500 μsec, indicating that the C=O stretching modes at core part and chiral part move in an opposite direction during the positive-voltage driving cycle.

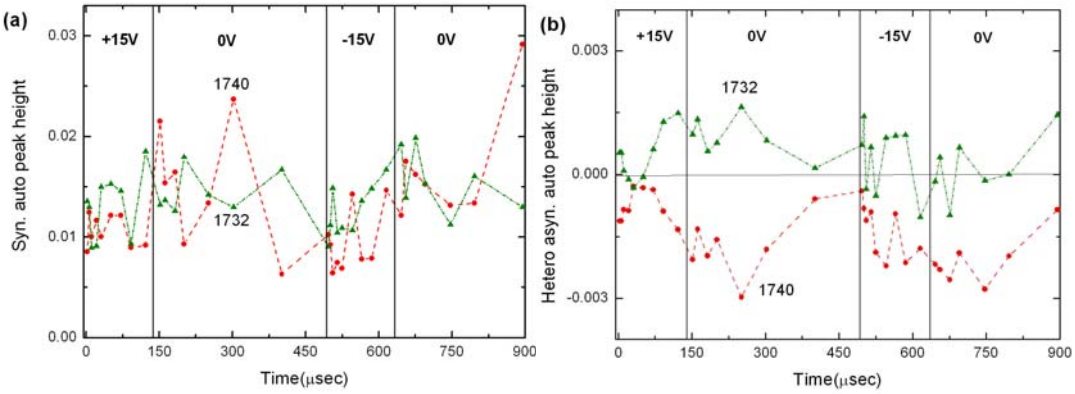

FIG. 6.14. Dynamic variations of (a) the 2D IR synchronous correlation, and (b) the hetero asynchronous correlation of C=O stretching modes.

We can use the time derivative of the hetero asynchronous correlation peaks to show the corresponding angular velocities. The results are presented in Fig. 6.15. By comparing Figs. 6.15(a) and 6.15(b), during the first 50 μsec of the negative field-on period, the angular velocities of both the C=O modes at 1732 and 1740 cm^{-1} exhibit rapid changes. The asymmetric response to positive and negative driving pulses is also observed in the C=C stretching modes at 1604 cm^{-1} shown in Fig. 6.13(b). It is found that within the initial 10 μsec after the rising edge of the applied field, the C=O stretching mode at 1732 cm^{-1} rotates with a slightly larger angular velocity than that at 1740 cm^{-1}, which appears to indicate that the field-induced reorientation of the CMHCB is led by the chiral part, and the molecular core follows. The alkyl chains and the vinyl groups are both insensitive to the external field and therefore no obvious reorientation can be detected. The observed phenomenon that the field-induced transient motions start from the chiral part is different from the result reported by Verma *et al.*, which mentioned that the

core part has an instantaneous response to the external field and the chiral part and alkyl chains response later.[26] The different result is believed to be caused by the different molecule structures used.

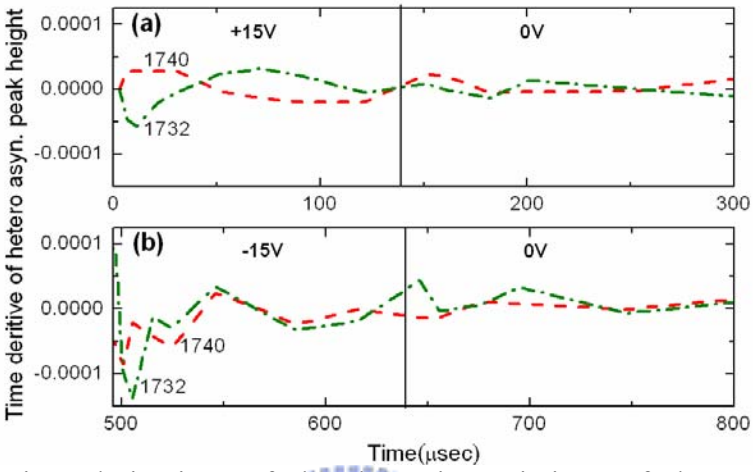

FIG. 6.15. Time derivatives of the dynamic variations of the 2D IR hetero asynchronous correlation in the (a) positive-voltage driving cycle and (b) negative-voltage driving cycle.

6.4 Summary

The effects of the isotropic term, the degree of uniaxial alignment, and the averaged apparent angle of a functional group in an anisotropic film on the 2D IR synchronous and asynchronous correlation were theoretically discussed. The results were employed to analyze the polarized IR spectra of a ferroelectric liquid crystal CMHCB in the K phase and SmC* phase. Our 2D correlation plots clearly reflect the exhibition of the thermal fluctuations in the azimuthal angle of the director about a tilt cone (Goldstone mode) in the SmC* phase. The phase-induced re-arrangement is found to depend on the molecular fragments. A time-resolved 2D IR correlation technique was applied to investigate the correlated motions of molecular segments in an electro-optic switching ferroelectric liquid crystal CMHCB. We demonstrated that the 2D IR correlation technique possesses useful

properties, which allow us to reveal clearly a field-induced collective reorientation of the molecular segments in the SSFLC. The reorientation process starts from the chiral part with an intramolecular motion, which proceeds in less than 10 μsec. In addition, an asymmetry in the response of the SSFLC to positive and negative driving pulses was also revealed in the 2D IR correlation analysis, indicating that the clockwise-anticlockwise symmetry about the cone axis is broken at the molecular level.

Chapter 7
2D IR Correlation Spectroscopy of an Electro-Optical Switching Ferroelectric Liquid Crystal Mixture

In Chapter 6, the combination of multichannel time-resolving system and the two-dimensional correlation spectroscopy is demonstrated to be a powerful tool for the investigation of molecular reorientation dynamics. An FLC mixture is studied to yield insight into correlated submolecular motions during the electro-optical switching process. Both 2D correlation analysis and the 2D hetero correlation analysis are applied to deduce the switching behavior of molecular fragments and to resolve the inter-molecular and intra-molecular motions. This chapter is organized as follows: The experimental details and the time-resolved IR spectra of an FLC mixture is presented first. Section 7.2.3 depicts the 2D correlation analysis results of the polarized IR spectra of the FLC mixture in the steady state. The analyses of time-resolved spectra with 2D correlation and 2D hetero correlation methods are discussed in Sec. 7.2.4.

7.1. Experimental Procedures

The SSFLC cells consist of two CaF_2 plates coated with indium tin oxide (ITO) conducting films and polyimide alignment layers rubbed unidirectionally. The substrates were assembled with 1.5 μm thick spacers, which is close to the

half-wave thickness $d_{\lambda/2}$ ~$\lambda/(2\Delta n)$ ~1.9 μm calculated with Δn ~0.17 and λ ~0.633 μm. An FLC mixture Felix 017/100 (Clariant, Frankfurt, Germany) with a phase sequence of $\text{Cr} \underset{-28\,^{\circ}C}{\leftrightarrow} \text{Sm-}C^{*} \underset{73\,^{\circ}C}{\leftrightarrow} \text{Sm-}A^{*} \underset{77\,^{\circ}C}{\leftrightarrow} N^{*} \underset{85\,^{\circ}C}{\leftrightarrow} \text{Iso}$ was chosen in view of its potential in industrial applications. The FLC material was filled into a test cell at a temperature above its isotropic phase and then the cell was allowed to slowly cool to 35 °C. All our SSFLC cells exhibit single domain under polarizing microscopic examination.

Time-resolved FTIR (trFTIR) spectra from 900 to 3500 cm^{-1} with 4-cm^{-1} resolution were recorded with a continuous-scan FTIR spectrometer equipped with a liquid nitrogen-cooled HgCdTe detector and a home-made data acquisition electronic system. Bipolar square-wave pulses were used to excite the SSFLC cell. The waveform includes a +10 V field-on duration extending from 0 to 140 μsec, followed by a field-free period from 140 to 500 μsec. Then a –10 V duration extends from 500 to 640 μsec, followed by a field-free period from 640 to 1000 μsec. For each polarization direction of the incident infrared light field, a total of 32 time-resolved interferograms were collected.[5]

7.2 Results and Discussion

7.2.1 Assignment of Infrared Absorption Bands

For the convenience of readers, infrared absorption spectra of the FELIX 017/100 FLC mixture and mode assignment are duplicated in Fig. 7.1. The FLC mixture can be viewed as an effective molecular system. From this view point, the IR spectral peaks at 1169, 1252, 1281, 1393, 1439, 1514, 1584, and 1608 cm^{-1} can be attributed to the normal modes associated with the cores; and the peaks at 2853, 2926, and 2956 cm^{-1} to the alkyl chains.[83] The highest-frequency peak at 2956 cm^{-1} is noted to originate from the anti-symmetric CH_3 stretching mode, whereas the two other peaks at 2853 and 2926 cm^{-1} are from the symmetric and anti-symmetric

CH_2 stretching along the alkyl chains. The peaks at 1608, 1584, 1547, 1514, and 1393 cm^{-1} are mainly from the C=C stretching modes of the benzene ring and the 1439-cm^{-1} peak could arise from the C=C stretch of pyrimidine ring. The remaining normal modes at 1169, 1254 (anti-sym), and 1281 (sym) cm^{-1} are associated with the C–O–C stretching modes.[83] In Fig. 7.1(b), the spectral peaks associated with the FLC cores are shown to yield an opposite angular dependence on the infrared polarization with those of alkyl chains.[84] A similar result had also been observed on neat FLC materials.[84] Note that these polarization-angle dependent patterns carry information about the averaged direction of IR dipoles. To gain more insight into the correlated motion of molecular segments, we apply 2D IR correlation to analyze the polarization-angle dependent patterns.

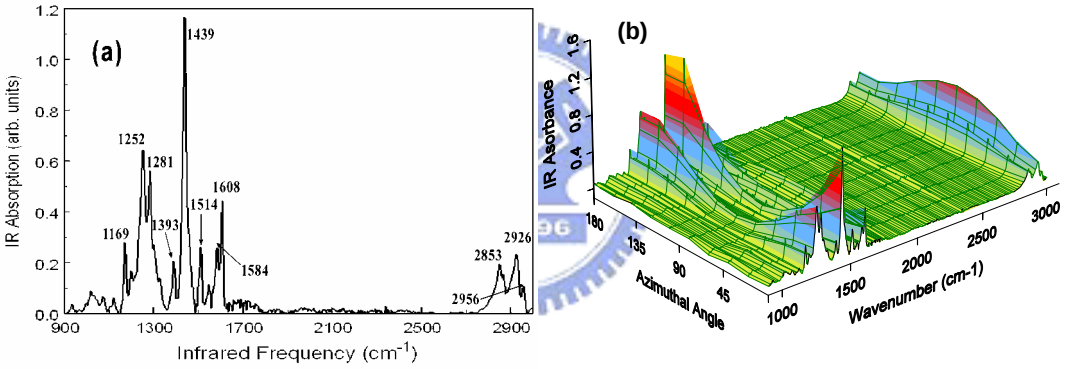

FIG. 7.1. (a) Infrared absorption spectrum of an SSFLC cell of FELIX 017/100 in SmC* at 35 °C; (b) A set of polarized IR spectra for the SSFLC cell at 35 °C and zero field for a number of polarizer rotation angles Φ in the range 0°–180°.

7.2.2 Time-Resolved Polarized FTIR Spectra

We had successfully acquired a set of time-resolved polarization-dependent IR absorption spectra of the electro-optical switching SSFLC. These spectra were used to deduce time-resolved polarization angle-dependent patterns for the observed IR peaks. The averaged apparent angles Φ_0 of the IR moments investigated and the corresponding dichroic ratios can be determined. The electro-optical responses of

the switching SSFLC can be probed by measuring the polarization-dependent transmittance. Similar to the IR spectra, the electro-optical responses were used to deduce the time-resolved polarization-angle dependent transmittance patterns and the averaged apparent angle of the SSFLC director. This method has been described in Chapter 5. The results are presented in Fig. 7.2.

Since our FLC material is a mixture with unknown molecular structures, an effective molecular system is proposed to explain the averaged response of each specific functional group, which could originate from various species. It is surprising to note that all apparent directions of the IR moments associated with the cores fall almost onto the same time course. The time course yields a response time of $\tau_{10\text{-}90}$=45 μsec, which is shorter than the electro-optical response time $\tau_{10\text{-}90}$=112 μsec (see the dashed curve of Fig. 7.2(a)). The electro-optical response can be estimated from $\tau = \gamma / P_s E_\perp$. Here γ denotes the rotational viscosity, P the spontaneous polarization of FLC and $E_\perp$ the applied electric field. By using the available material parameters of Felix 017/100: $\gamma = 8\times10^{-6}\, N\cdot \sec/cm^2$, $P_s = 10.5\ nC/cm^2$, and the applied field strength $E_\perp = 6.7\times10^4\, V/cm$, we obtain $\tau = 114\ \mu\sec$. The value agrees very well with the observed electro-optical response time of the SSFLC. Since the FLC director is inseparably coupled to its polarization, there will be a collective reorientation of the molecules according to the field direction. However, the field response of molecular fragments could be faster than the electro-optical response time.

The dichroic ratio of the C=C stretch at 1608 cm^{-1}, normalized to the initial dichroic ratio at *t* = 0 μsec, reaches a peak at *t* = 70 μsec after the rising edge of the positive applied field (see Fig. 7.2(b)). Significant rapid variations were also observed near the transition edge of the applied field. The C–O–C stretching mode at 1252 cm^{-1} exhibits similar but less distinctive variation in the dichroic ratio. Although the variation of dichroic ratio with dc voltage had been observed on a neat FLC material,[87] our FLC mixture shows that the variation can occur during

both the voltage-holding periods and the field-free periods. Considering that each observed IR absorption peak in this study can originate from atomic groups which belong to different species, our result thus suggest that the C=C fragments of different molecules in the FLC mixture do not move in unison during the electric field-induced reorientation process. Notably, the dichroic ratio changes of different IR stretching modes in the positive-voltage cycle are different from those in the negative-voltage cycle, indicating that the molecular distributions should also depend on the polarity of the applied field.

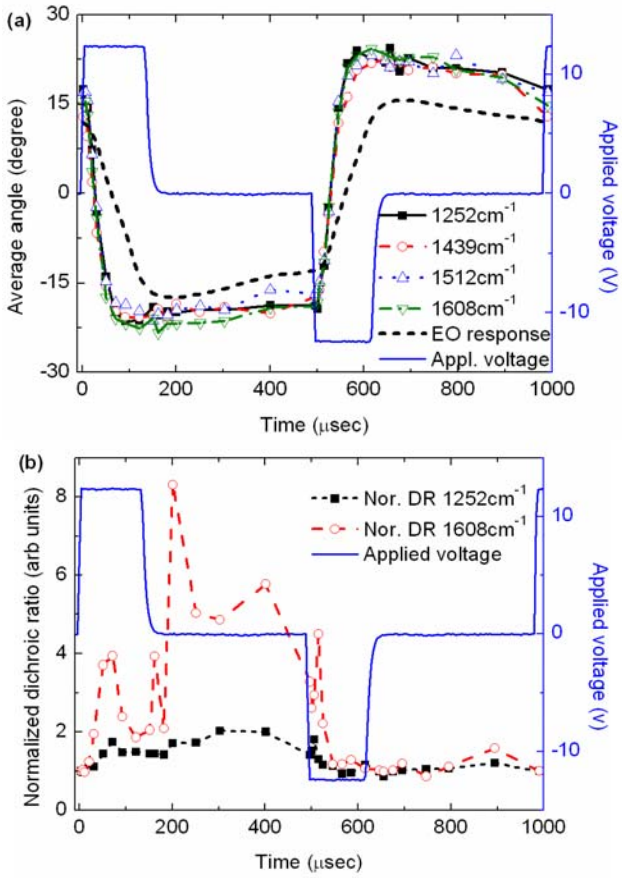

FIG. 7.2. (a) The dynamic variation curve of the electro-optical response (dashed curve) and the average apparent angles of selected IR absorption peaks associated with the core segments (symbols); (b) the time courses of the dichroic ratios of the C=C stretch mode at 1608 cm^{-1} (open symbols) and C–O–C stretch at 1252 cm^{-1} (filled symbols). The waveform of the bipolar driving pulses is also included for reference.

Figure 7.3 presents a comparison of the dichroic ratio (open symbols) and the synchronous auto peak (solid symbols) of the C=C stretching mode at 1608 cm^{-1} and the C–O–C motion at 1252 cm^{-1}. High correlation was observed for these two normal modes, which are associated with the LC cores. The time course of the synchronous auto peak (see the solid squares of Fig. 7.3(b)) at 1608 cm^{-1}, which agrees very well with the variation of the dichroic ratio. It exhibits the first peak at 70 μsec after the rising edge of the positive pulse. At this instant, the averaged apparent angles of all the core functional groups reach their extreme value (see Fig. 7.2(a)). The second maximum of the synchronous auto peak occurs at 170 μsec, where the electro-optical signal of the SSFLC also reaches an extreme value. Significant variations in both the dichroic ratio and the synchronous auto peak were observed near 500 μsec, where the negative field is just switched on. Minor differences between the dichroic ratio and the synchronous auto peak can still be detected. The deviations could be attributed to originate from the isotropic component of the film, which has an effect on the dichroic ratio but can not affect the synchronous auto peak (see Sec. 6.2).

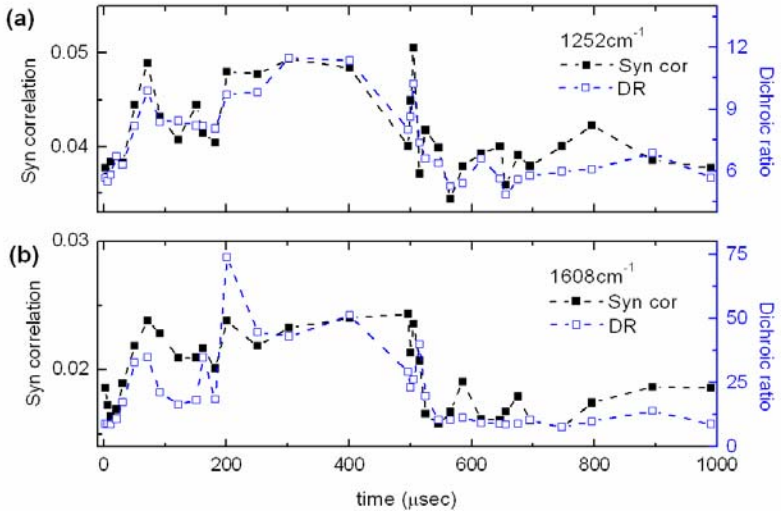

FIG. 7.3. Comparison of the dichroic ratios (open symbols) and the 2D IR synchronous auto peak (filled symbols) of (a) C–O–C stretch at 1252 cm^{-1}, and (b) C=C stretch mode at 1608 cm^{-1}.

7.2.3 2D Polarized IR Correlation Analysis of the FLC Mixture in Steady State

In this section, the polarized IR spectrum measured in steady state as well as the time-resolved polarized IR spectrum measured in switching state are analyzed by the 2D correlation spectra. The theoretical consideration has already been presented in Sec. 6.2.

The left column of Fig. 7.4 shows the 2D synchronous correlation spectra in the 1500–1620 cm^{-1} region, generated from the FLC mixture without an electric field (Fig. 7.4(a)), with +5 V (Fig. 7.4(c)) and –5 V (Fig. 7.4(e)) electric field. Note that three auto peaks are formed at 1514, 1584, and 1608 cm^{-1}. These peaks correspond to the C=C stretching modes with the transition moments coincide with that of the benzene ring. These peaks also yield significant cross peaks, indicating a strong correlation existing among these modes.

The appearance of asynchronous cross peaks sensitively reflects the relative orientation changes of the vibrational modes. The asynchronous 2D correlation plots without an applied field (Fig. 7.4(b)) and with +5 V (Fig. 7.4(d)) and –5 V (Fig. 7.4(f)) are shown on the right column of Fig. 7. The asynchronous cross peaks are quite distinctive without an applied field, indicating that significant orientational deviation may exist among these C=C stretching modes. The asynchronous cross peak features become much less distinctive when an electric field is applied (see Figs. 7.4(d) and 7.4(f)). This phenomenon can be understood by noting that for the SmC* phase with unwound structure, the thermal fluctuations in the azimuthal angle ϕ of the director about a tilt cone (i.e., the Goldstone mode) can be suppressed by an external electric field and the molecular tilt plane is parallel to the cell substrates.[85,86] This configuration could lead to a reduction of the degree of freedom and therefore a decrease of the orientational deviation of molecular fragments.

We also detect some field polarity-induced differences in the asynchronous

cross peaks. For example, the cross peak in Fig. 7.4(f) at 1514 cm^{-1} relative to 1584 and 1608 cm^{-1} are more distinctive when a negative electric field is applied. The asymmetry with positive and negative fields indicates that the clockwise-anticlockwise symmetry is broken at the submolecular level in this FLC mixture.

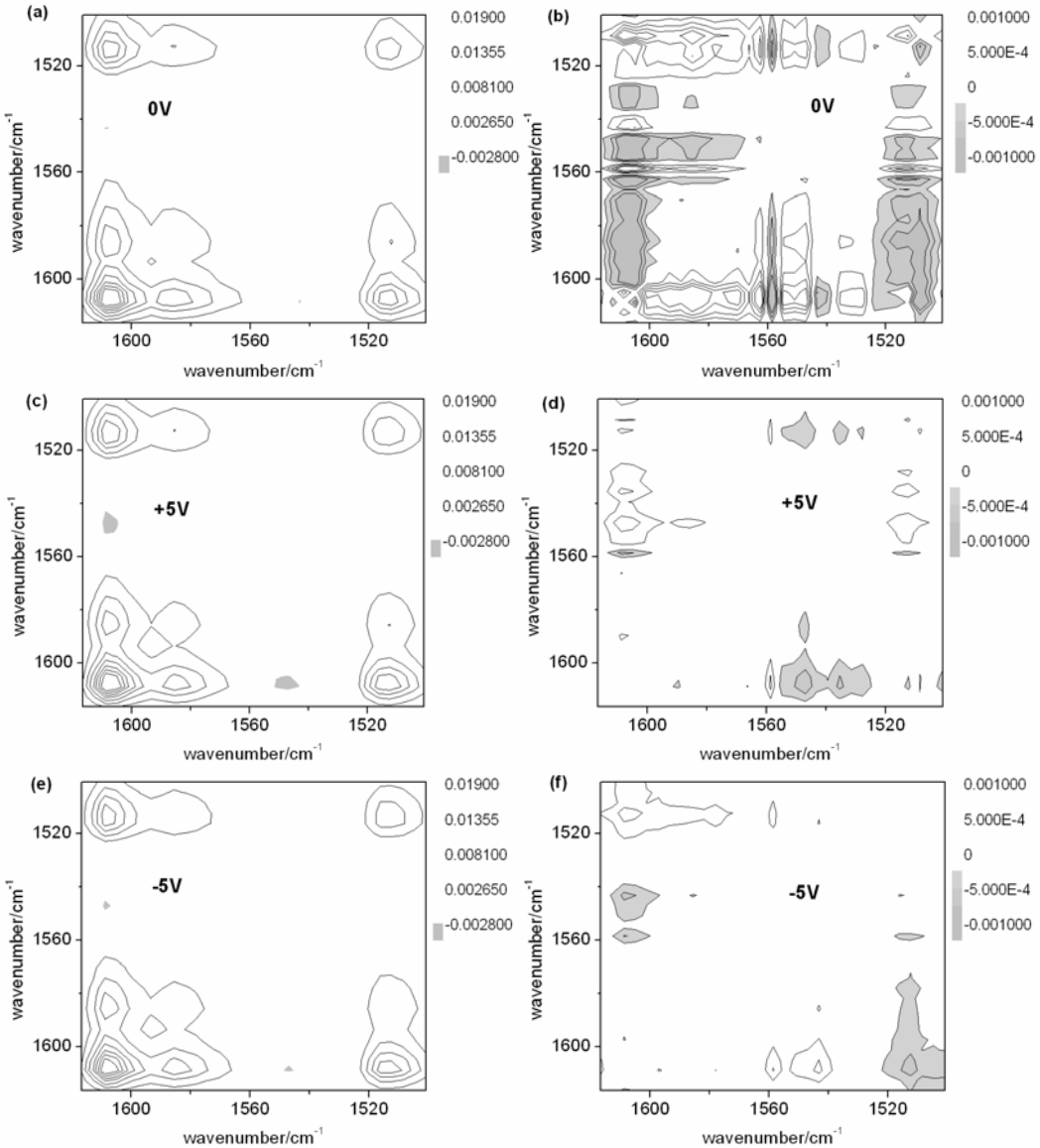

FIG. 7.4. (Left column: a, c, e) Synchronous 2D IR correlation spectrum in the 1620–1500 cm^{-1} region generated from the polarization-angle dependent from 0° to 180° polarized spectral variations of FELIX 017/100 in SmC* at 35 °C (a) without an external field, (c) applying DC +5 V, and (e) –5 V; (Right column: b, d, f) the corresponding 2D IR asynchronous correlation spectrum in the 1620–1500 cm^{-1} region.

7.2.4 Time-Resolved 2D IR Correlation Analysis of the Switching Dynamics of the FLC Mixture

The switching dynamics of an SSFLC mixture can be better understood by monitoring the field-induced reorientation of different molecular segments with trFTIR. The obtained time-resolved polarization angle-dependent patterns of infrared absorption peaks are subject to 2D hetero correlation and 2D correlation analyses and the time courses of the synchronous and the asynchronous peaks are yielded. Notably, the hetero asynchronous correlation analysis can reflect the transient fragmental reorientations of the switching states to that in the original field-free orientation. The 2D asynchronous correlation analysis provides the information about the transient angular deviations between two molecular fragments at each time slice. By combining these two pieces of information together, the correlated motions of molecular fragments in the FLC material can be resolved unambiguously.

Time courses of 2D IR hetero asynchronous auto-peaks are shown in Fig. 7.5(a). Note that the zero hetero asynchronous correlation denotes that at this instant the transient orientation of a molecular segment is along to its field-free virgin direction. The hetero asynchronous auto peaks of the molecular segments change from negative to positive values during the positive driving cycle, and during the negative driving cycle the corresponding peaks change from positive to negative values. The changes of the signs and the values of the auto peaks imply that the field-induced reorientations of the molecular segments point to the opposite sides of their field-free virgin directions with different and asymmetric angles. The expanded view shown in Fig. 7.5(b) indicates that all molecular segments except the 2924 cm^{-1} mode cross the zero hetero asynchronous hetero correlation point at the instant of 32 μsec, thus supports the picture of a collective reorientation of the molecular fragments.

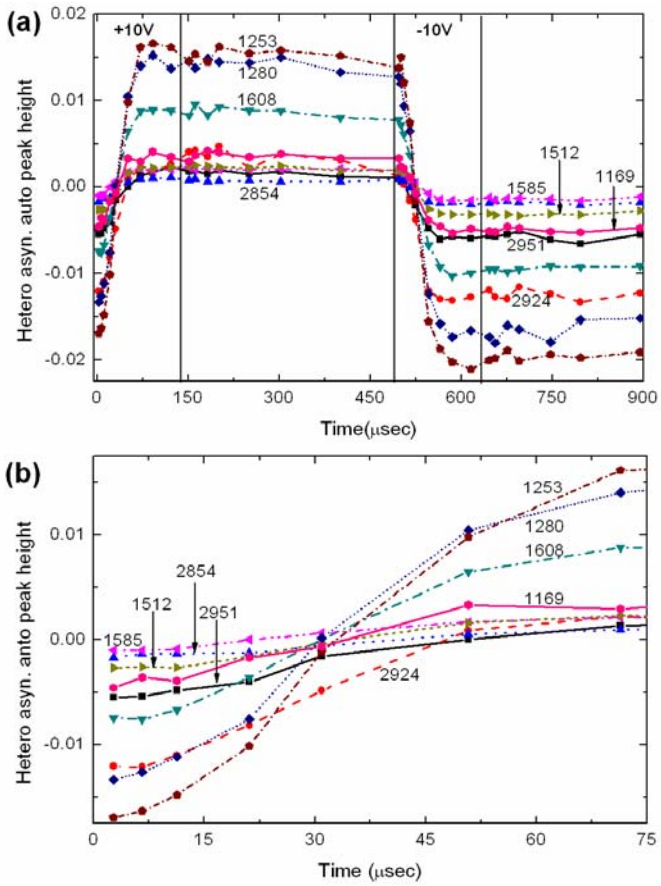

FIG. 7.5. (a) Time courses of 2D IR hetero asynchronous auto peaks generated from the time-resolved polarization-angle dependent spectra of FELIX 017/100 at 35 °C; (b) the expanded view of (a) near the rising edge of the positive driving pulse.

We can calculate the time derivative of the hetero asynchronous correlation peaks to reveal the corresponding angular velocities of molecular fragments. The results are presented in Fig. 7.6. It is found that during the positive driving cycle, the angular velocities of all molecular segments increase rapidly and reach a peak velocity at about $t_{\phi=90} = 30\mu\,\mathrm{sec}$. When the field is switched off, the angular velocities exhibit a damped oscillation behavior and finally settle down to zero near 250 μsec. The time courses of angular velocities shown in Figs. 7.5(a) and 7.6 clearly separate into the three groups of C–O–C, C=C, and alkyl chains. The C–O–C stretching modes exhibit the highest angular velocity, while the C=C stretching modes rank the second and CH_2/CH_3 stretching modes are the third.

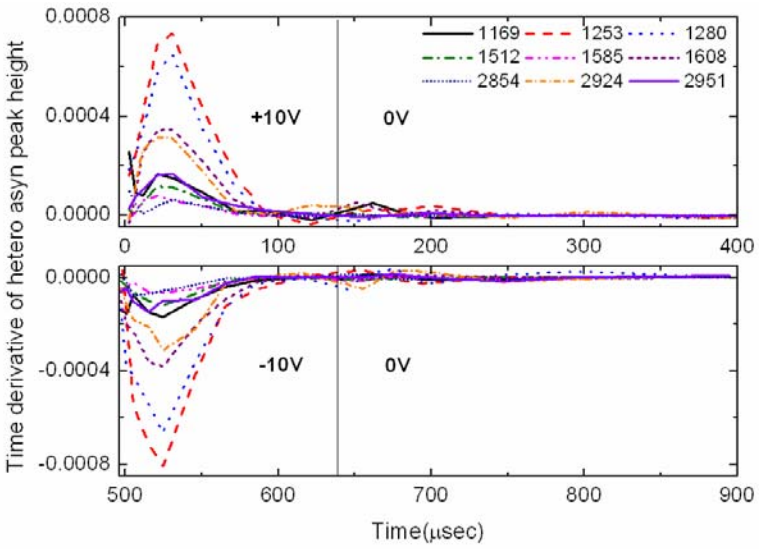

FIG. 7.6. Time derivatives of the dynamic variations of the 2D IR hetero asynchronous correlation in positive-voltage driving cycle (top) and negative-voltage driving cycle (bottom).

The alignments and relative motions between the molecular segments of an SSFLC mixture can be deduced by subjecting the obtained time-resolved polarization angle-dependent patterns of infrared absorption peaks to 2D correlation analysis. The time courses of the asynchronous cross peaks of the C=C stretching modes and the C–O–C stretching modes relative to the one at 1609 cm^{-1} are presented in Figs. 7.7(a) and 7.7(b). It is interesting to note that in Fig. 7.7(a) the cross peaks of all other C=C stretching modes are higher than the 1609 cm^{-1} mode from 0 to 500 μsec and they become lower than the 1609 cm^{-1} mode during the negative-voltage driving cycle. Based on the previous theoretical analysis, we can conclude that all the C=C stretching modes relative to the 1609 cm^{-1} mode are rotated on the SmC* cone with a smaller apparent angle during the positive-voltage driving cycle and with a larger apparent angle during the negative-voltage driving cycle. This suggest that the during the switching processes, the FLC molecule not only rotates around the layer normal, but also revolves around the molecular long axis. Similar phenomenon in a neat FLC material also has been reported by Zhao *et al.* in 2002.[79] The C–O–C modes (shown in Fig. 7.7(b)) yield similar results for the synchronous cross peaks. But the asynchronous cross peaks of the C–O–C

stretching modes exhibit higher degree of fluctuation, indicating a more random switching behavior than the C=C stretching mode at 1609 cm^{-1}.

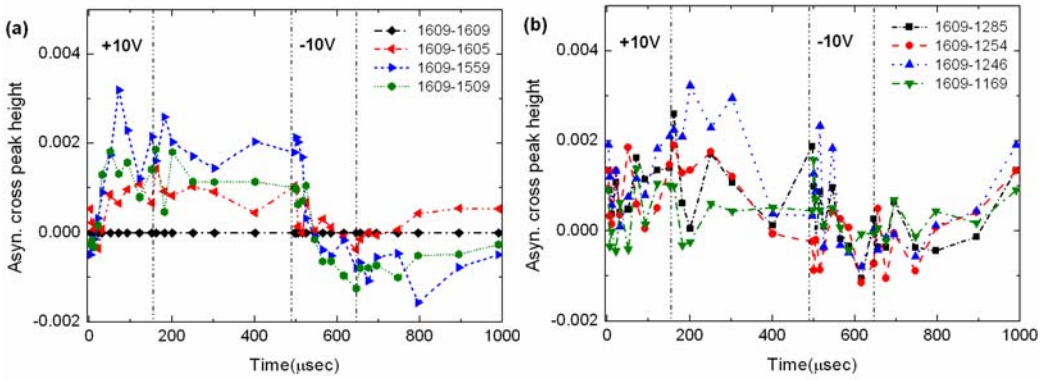

FIG. 7.7. Dynamic variations of the 2D IR asynchronous correlation of (a) C=C stretching modes and (b) C–O–C stretching modes with respect to the C=C stretching mode at 1609 cm^{-1}.

Note that the asynchronous cross peak heights shown in Figs. 7.7(a) and 7.7(b) reflect the angular deviations from that along to the C=C stretching mode at 1609 cm^{-1}. It is therefore convenient to define an angular spread of the molecular core part by summing all the asynchronous cross peak heights that are associated to the cores. The results are presented in Fig. 7.8. A rapid variation in the angular spread parameter can be found during the initial 30 μsec (stage-I) after a positive electric field is switched on. Immediate to the stage-I, a gradual but more significant variation is developed while the applied electric field is still on (stage-II). The significant variation persists even the applied field is turned off (stage-III). When the applied field is negative, the angular spread variation during the stages II and III becomes much less significant. The considerable differences of the angular spread between the three stages imply that the molecules could undergo different types of molecular motions in these stages.

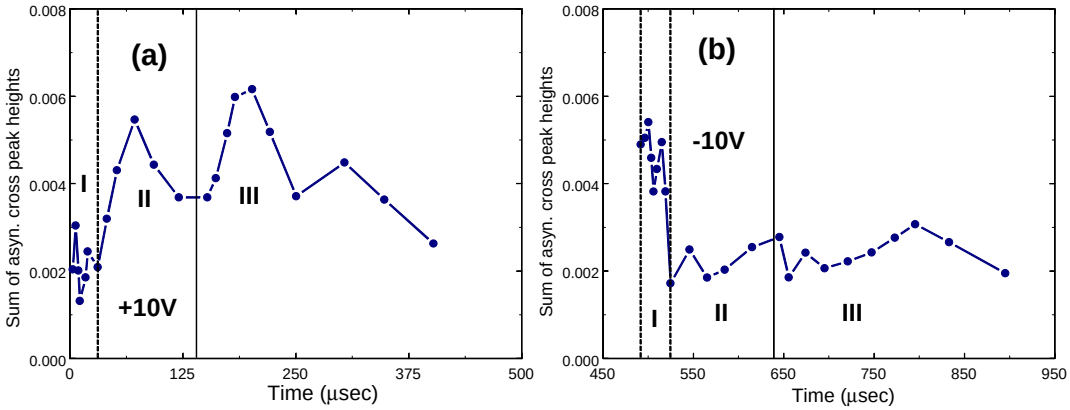

FIG. 7.8. Dynamic variation of the angular spread of the functional groups (C=C and C–O–C) associated with the core segments relative to that along to the C=C stretching mode at 1608 cm^{-1} is plotted for (a) the +10 V pulse driving, (b) the –10 V pulse driving. Stage I and II denote the field-on duration and stage III is the field-off period.

To further investigate the mutual molecular motions in the three stages mentioned above, the 2D hetero synchronous correlation analysis of the IR spectra between the field-free virgin states and the field-induced transient states is introduced to deduce the alignment status of the orientation of the molecular segments. The 2D hetero synchronous auto-peaks of the vibrational normal modes associated with the cores of the molecular species are presented in Figs. 7.9(a) and 7.9(b). We first noted that the molecular fragments have higher synchronous hetero correlations (therefore a higher degree of uniaxial alignment) during the positive driving cycle. During the positive driving cycle, the hetero synchronous auto peak at 1608 cm^{-1} displays the first maximum at 30 μsec after the rising edge of the positive pulse; while the stretching modes at 1253 and 1280 cm^{-1} reach their first peaks with a slightly longer time period of 60 μsec. The result can be caused by the more rigid nature of the C=C stretching mode at 1608 cm^{-1} and thus faster field-induced reorientation.

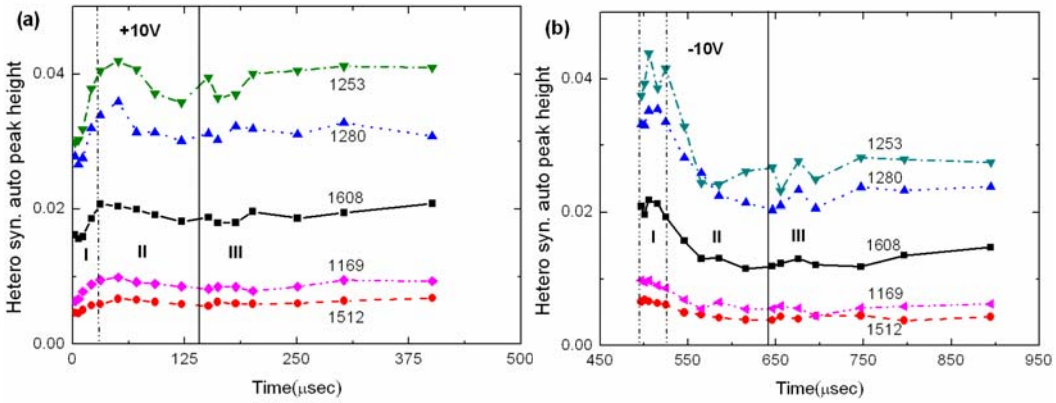

FIG. 7.9. The time courses of 2D IR hetero synchronous auto peaks generated from the time-resolved polarization-angle dependent spectra from 0° to 180° of FELIX 017/100 at 35 °C during (a) the positive voltage driving cycle and (b) the negative voltage driving cycle. Stage I and II denote the field-on duration and stage III is the field-off period.

Combining the information provided from Figs. 7.8 and 7.9, the transient motions of the molecules can be understood as follows. Similar to the stages shown in the dynamic analyses of the angular spread of the segments associated with molecular core, we also divide the time courses of 2D hetero synchronous auto peaks into three stages, which are presented in Fig. 7.9. Since in stage I the observed variations of angular spread are rapid but relatively small, we attribute that to from the field-induced intramolecular motions. The hetero synchronous correlations observed in stage I almost preserve their peak values at the first 10 microseconds, indicating that the mutual fragmental motions start from the functional groups attached to single molecule. While the applied field in on, the hetero synchronous correlations begin to change and therefore the correlated motions propagate from the molecular fragments belonging to single molecule to those of other surrounding molecules. However, in stage II, the gradual variation in the angular spread and the hetero synchronous correlations could originate from that a larger degree of freedom is allowed for the field-induced intermolecular motion. The variation in angular spread persists even when the field is switched off. When the applied field is negative, the intermolecular motion was found to be much weaker during the stage III. The asymmetry with positive and negative

driving pulses is also observed in the 2D correlation plot shown in Fig. 7.4.

7.3 Summary

In this chapter, time-resolved infrared two-dimensional correlation (2DC) spectroscopy and a time-resolved 2D IR hetero correlation technique (2DHC) have been employed to analyze an electro-optic switching FLC mixture.

The 2DC analysis clearly reveals that the thermal fluctuations in the azimuthal angle of the FLC director about a tilt cone (Goldstone mode) in the SmC* phase with unwound structure are suppressed by an applied electric field. In addition, an asymmetry in the response of the SSFLC mixture to positive and negative driving pulses was also revealed in the 2DC analysis, indicating that the clockwise-anticlockwise symmetry about the cone axis is broken at the molecular level in the FLC mixture. Moreover, we had also applied 2DHC technique to investigate the correlated motions of molecular segments. We demonstrated that the 2DHC technique possesses useful properties, which allow us to reveal clearly a field-induced collective reorientation of the molecular segments in the SSFLC. In a transient situation, the field-induced reorientation process was found to start with an intramolecular motion, which proceeds in about 10 μsec. The intramolecular motion then propagates from the fragments attached to a single molecule to the ones belonging to different molecular coordinates. The molecular segments of C–O–C, C=C, and C–H stretch modes were found to rotate about a tilted cone with different angular speeds in a correlated but non rigid way.

Chapter 8
Conclusion
and Future Prospect

In conclusion, the field-induced molecular reorientation dynamics of a nematic twisted pi-cell and SSFLCs have been studied by time-resolved polarized FTIR and Raman spectroscopy. We constructed a multichannel time resolving system to perform the time-resolved FTIR measurements. 2D correlation analysis was employed to further explore the molecular conformations and reorientations from the information provided by the obtained complex IR spectra. The different information obtained from the 2D correlation (2DC) technique and 2D hetero correlation (2DHC) technique was elucidated. To gain more knowledge about the 2D correlation spectroscopy, the effects of the isotropic terms, the degrees of uniaxial alignments, and the averaged apparent angles of functional groups in an anisotropic film on the 2D synchronous and asynchronous correlation were theoretically discussed.

A nematic twisted pi-cell has been studied by optical transmission measurement, polarized Fourier transform infrared (pFTIR) absorption spectroscopy, and time-resolved Raman spectroscopy. The alignment of the LC molecules was revealed. Our results suggest that the molecules undergo a restricted rotation about the molecular long axis. The rise and decay times of the electro-optical response were found to be 6 ms and 1.6 ms, respectively. In the switching dynamic process, our data show that LC molecules in the twisted pi-cell do not rotate like a rigid molecule during the field induced reorientation process.

The molecular conformations and alignments of a neat ferroelectric liquid crystal CMHCB in the K phase and SmC* phase were studied by 2D polarized IR

spectra. The 2D IR correlations clearly reflect the exhibition of Goldstone mode in the SmC* phase. The phase-induced re-arrangement is found to be dependent on the molecular fragments. We demonstrated that by the 2D IR correlation technique, a field-induced collective reorientation of the molecular segments in the SSFLC can be reveal. The reorientation process starts from the chiral part with an intramolecular motion, which proceeds in less than 10 μsec. In addition, we found an asymmetry in the response of the SSFLC to positive and negative driving pulses, indicating that the clockwise–anticlockwise symmetry about the cone axis is broken at the molecular level in CMHCB.

The molecular motion of an SSFLC mixture during a field-induced reorientation process was studied by time-resolved electro-optical response measurements. The FLC director investigated can respond rapidly to a pulsed driving field, while the orientation distribution was found to spread at first and then slowly converge to the new direction of the FLC director. In regard to the submolecular behaviors, the 2DC analysis clearly reveals that the thermal fluctuations in the azimuthal angle of the FLC director about a tilt cone (Goldstone mode) in the SmC* phase with unwound structure are suppressed by an applied electric field. In addition, an asymmetry in the response of the SSFLC mixture to positive and negative driving pulses was also revealed in the 2DC analysis, indicating that the clockwise–anticlockwise symmetry about the cone axis is broken at the molecular level in the FLC mixture. Moreover, by the 2DHC technique, the correlated motions of molecular segments were investigated. We demonstrated that the 2DHC technique possesses useful properties, which allow us to reveal clearly a field-induced collective reorientation of the molecular segments in the SSFLC. In a transient situation, the field-induced reorientation process was found to start with an intramolecular motion, which proceeds in about 10 μsec. The intramolecular motion then propagates from the fragments attached to a single molecule to the ones belonging to different molecular coordinates. The molecular segments of C–O–C, C=C, and C–H stretch modes were found to rotate about a

tilted cone with different angular speeds in a correlated but non rigid way.

We believe that the combination of the multichannel time-resolved vibrational spectroscopy and the 2D correlation spectroscopy shall be useful for complete characterizing various phenomenon, such as the studies of field-induced transient molecular deformations and alignment, submolecular dynamics and molecular-environment interactions. The 2D hetero spectra correlation, for example, between the IR absorption and sum frequency vibrational spectroscopy, can be performed to deduce more information behind a phenomenon of interest. In the future investigation of liquid crystal materials, studies of a mixture with well known molecular structures are believed to yield definite details of the molecular reorientation dynamics.

Bibliography

1. S. -H. Chen and C. L. Yang , Appl. Phy. Lett. **80,** 3721 (2002).
2. R. B. Meyer, L. Liebert, L. Strzelecki, and P. Keller, Le Journal De Physique Letters **36**, L69 (1975).
3. N. A. Clark and S. T. Lagerwall, Appl. Phys. Lett. **36**, 899 (1980).
4. L. M. Blinov and V. G. Chigrinov, *Electrooptic Effects in Liquid Crystal Materials* (Springer-Verlag, New York, 1994), p.459.
5. K. Masutani, H. Sugisawa, A. Yokota, Y. Furukawa, and M. Tasumi, Appl. Spectrosc. **46**, 560 (1992).
6. K. Masutani, K. Numahata, K. Nishimura, S. Ochiai, Y. Nagasaki, N. Katayama, and Y. Ozaki, Appl. Spectrosc. **53**, 588 (1999).
7. I. Noda, A. E. Dowrey, C. Marcott, G. M. Story, and Y. Ozaki, Appl. Spectrosc. **54**, 236A (2000).
8. Wen-Tse Shih and Jung Y. Hunag, Liq. Cryst. **29**, 283 (2002).
9. W. T. Shih, J. Y. Huang, and J. Y. Zhang, Liq. Cryst. **31**, 377 (2004).
10. P. J. Collings, *Liquid Crystals* (IOP Publishing Ltd, 1990).
11. P. J. Collings and M. Hird, *Introduction to Liquid Crystals: Chemistry and Physics* (CRC Press, London, 1997).
12. D. Demus, J. W. Goodby, G. W. Gray, H.-W. Spiess, and V. Vill, *Handbook of Liquid Crystals* (Wiley-VCH, Weinheim, 1998).
13. P. Yeh and C. Gu, *Optics of Liquid Crystal Displays* (John Wiley & Sons, New York, 1999).
14. P. J. Bos, R. Koehler, and K. Beran, Mol. Cryst. Liq. Cryst. **113,** 329 (1984).
15. T. Miyashita, C. L. Kuo, and T. Uchida, SID '95, 797, (1995).
16. H. Nakamura and M. Noguchi, Jpn. J. Appl. Phys. **39,** 6368 (2000).
17. P. Maltese, R. Piccolo, and V. Ferrara, Liq. Cryst. **15(6)**, 819 (1993).

18. C. Escher, H. R. Dübal, T. Harada, G. Illian, M. Murakami, and D.Ohlendorf, Ferroelectrics **113**, 269 (1991).
19. C. Escher, T. Gelhaar, and E. Böhm, Liq. Cryst. **3(3)**, 469 (1988).
20. J. C. Jones, M. J. Towler, and E. P. Raynes, Ferroelectrics **121**, 91 (1991).
21. W. G. Jang and N. A. Clark, Phys. Rev. E **63**, 031707 (2001).
22. F. Hide, N. A. Clark, K. Nito, A. Yasuda, and D. M. Walba, Phys. Rev. Lett. **75**, 2344 (1995).
23. A. L. Verma, B. Zhao, S. M. Jiang, J. C. Sheng, and Y. Ozaki, Phys. Rev. E **56**, 3053 (1997).
24. S. V. Shilov, H. Skupin, F. Kremer, E. Gebhard, and R. Zentel, Liq. Cryst. **22**, 203 (1997).
25. A. Kocot, R. Wrzalik, B. Orgasinska, T. Perova, J. K. Vij, and H. T. Nguyen, Phys. Rev. E **59,** 551 (1999).
26. A. L. Verma, B. Zhao, H. Terauchi, and Y. Ozaki, Phys. Rev. E **59,** 1868 (1999).
27. B. Schrader and D. Bougeard, *Infrared and Raman Spectroscopy: Methods and Applications* (Wiley-VCH, Weinheim, 1995).
28. L. T. Letendre, H. -L. Dai, I. A. McLaren, and T. J. Johnson, Rev. Sci. Instrum. **70**, 18 (1999).
29. J. Lindner, J. K. Lundberg, R. M. Williams, and S. R. Leone, Rev. Sci. Instrum. **66** (4), 2812 (1995).
30. W. S. Neil, J.-Y. Li, J. J. Sloan, and F.-A. Kong, J. Chem. Phys. **107**, 4537 (1997).
31. J. Lindner, R. A. Loomis, J. J. Klaassen, and S. R. Leone, J. Chem. Phys. **108**, 1944 (1998).
32. H. C. Wang, R. A. Palmer, and C. J. Manning, Appl. Spectrosc. **51**, 1245 (1997).
33. R. V. Kasza, J. G. Shapter, K. Griffiths, P. R. Norton, and J. J. Sloan, Surf. Sci. **321**, L239 (1994).
34. S. R. Leone, A. Chem. Res. **22**, 139 (1989).

35. S. A. Rogers and S. R. Leone, Appl. Spectrosc. **47**, 1430 (1993).
36. G. Hancock and D.E. Heard, in *Advances in Photochemistry*, edited by D.H. Volman, G. S. Hammond, and D. C. Neckers (Wiley, New York, 1993), Vol. 18, pp. 1-65.
37. J. J. Sloan and E. J. Kruus, in *Advances in Spectroscopy*, Vol. 18, *Time-Resolved Spectroscopy*, edited by R. J. H. Clark and R. E. Hester (Wiley, New York, 1989), pp. 219-253.
38. P. W. Seakins, in *The Chemical Dynamics and Kinetics of small Radicals*, Part I, *Advanced Serious in Physical Chemistry*, edited by K. Liu and A. Wagner (World Scientific, Singapore, 1995). Vol. 6, pp. 250-314.
39. J. Lindner, O. Stahlhut, R. Wihelm, and K. Ermisch, Rev. Sci. Instrum. **69**, 1629 (1998).
40. G. V. Hartland, W. Xie, H. -L. Dai, A. Simon, and M. J. Anderson, Rev. Sci. Instrum. **63**, 3261 (1992).
41. G. Durry and G. Guelachvili, Appl. Opt. **34**, 1971 (1995).
42. G. Durry and G. Guelachvili, J. Opt. Soc. Am. B **12**, 1555 (1995).
43. C. A. Carere, W. S. Neil, and J. J. Sloan, Appl. Opt. **35**, 2857 (1996).
44. R. A. Palmer, C. J. Manning, J .L. Chao, I. Noda, A. E. Dowrey, and C. Marcott, Appl. Spectrosc. **45**, 12 (1991).
45. W. Uhmann, A. Becker, C. Taran, and F. Siebert, Appl. Spectrosc. **45**, 390 (1991).
46. R. A. Palmer, J. L. Chao, R. M. Dittmar, V. G. Gregoriou, and S. R. Plunkett, Appl. Spectrosc. **47**, 1297 (1993).
47. K. Masutani, A. Yokota, Y. Furukawa, M. Tasumi, and A. Yoshizawa, Appl. Spectrosc. **47**, 1370 (1993).
48. M. A. Czarnecki, N. Katayama, Y. Ozaki. M. Satoh, K. Yoshio, T. Watanabe, and T. Yanagi, Appl. Spectrosc. **47**, 1382 (1993).
49. M. A. Czarnecki, N. Katayama, M. Satoh, T. Watanabe, and Y. Ozaki, J. Phys. Chem. **99**, 14101 (1995).

50. K. H. Kim, K. Ishikawa, H. Takezoe, and A. Fukuda, Phys. Rev. E **51**, 2166 (1995).
51. B. Jin, Z. Ling, Y. Takahashi, K. Ishikawa, H. Takezoe, A. Fukuda, M. Kakimoto, and T. Kitazume, Phys. Rev. E **53**, R4295 (1996).
52. N. Katayama, M. A. Czarnecki, M. Satoh, T. Watanabe, and Y. Ozaki, Appl. Spectrosc. **51**, 487 (1997).
53. W. P. Aue, B. Bartholdi, and R. R. Ernst, J. Chem. Phys. **64**, 2229 (1976).
54. A. Bax, *Two Dimensional Nuclear Magnetic Resonance in Liquids* (Reidel, Boston, 1982).
55. R. R. Ernst, G. Bodenhausen, and A. Wakaun, *Principles of Nuclear Magnetic Resonance in One and Two Dimensions* (Oxford University Press, Oxford, 1987).
56. J. K. M. Sanders and B. K. Hunter, *Modern NMR Spectroscopy: A Guide for Chemists* (Oxford University Press, New York, 1993).
57. I. Noda, Bull. Am. Phys. Soc. **31**, 520 (1986).
58. I. Noda, J. Am. Chem. Soc. **111**, 8116 (1989).
59. I. Noda, Appl. Spectrosc. **44**, 550 (1990).
60. I. Noda, Appl. Spectrosc. **47**, 1329 (1993).
61. Y. Ozaki and I. Noda, *Two-Dimensional Correlation Spectroscopy* (American Institute of Physics, New York, 2000).
62. Y. Ozaki and I. Noda, in *Encyclopedia of Analytical Chemistry*, edited by. R. A. Meyers (John Wiley & Sons, Chichester, 2000), p. 322.
63. I. Noda, in *Modern Polymer Spectroscopy*, edited by G. Zerbi (Wiley-VCH, Weinheim, 1999).
64. I. Noda, in *Handbook of Vibrational Spectroscopy Vo1. 3*, edited by J. M. Chalmers and P. R. Griffiths (John Wiley & Sons, Chichester, 2002).
65. Y. Ozaki, in *Handbook of Vibrational Spectroscopy Vo1. 3*, edited by J. M. Chalmers and P. R. Griffiths (John Wiley & Sons, Chichester, 2002).
66. Y. Ozaki, S. Šašic, T. Tanaka, and I. Noda, Bull. Chem. Soc. Jpn. **74**, 1 (2001).

67. Y. Ozaki, S. Šašic, and J. -H. Jiang, J. Near Infrared Spectrosc. **9**, 63 (2001).
68. Y. Ozaki and S. Šašic, in *Vibrational Spectroscopy of Biological and Polymeric Materials*, edited by M. Braiman and V. Gregoriou (Marcel Dekker, New York, in press).
69. I. Noda, Appl. Spectrosc. **54**, 994 (2000).
70. N. Hayashi and T. Kato, Phys. Rev. E **63,** 21706 (2001).
71. B. Delley, in *Density Functional Methods in Chemistry*, edited by J. K. Labanowskiand and J. W. Andzelm (Springer Verlag, New York, 1991).
72. H. Skupin, F. Kremer, S. V. Shilov, P. Stein, and H. Finkelmann, Macromolecules **32**, 3746 (1999).
73. A. A. Sigarev, J. K. Vij, Yu. P. Panarin, and J. W. Goodby, Phys. Rev. E **62,** 2269 (2000).
74. W. G. Jang, C. S. Park, and N. A. Clark, Phys. Rev. E **62**, 5154 (2000).
75. W. G. Jang, C. S. Park, K. H. Kim, M. A. Matthew, A. Glaser, and N. A. Clark, Phys. Rev. E **62**, 5027 (2000).
76. S. T. Lagerwall, *Ferroelectric and Antiferroelectric Liquid Crystals* (Wiley-VCH, Weinheim, 1999).
77. D. M. Walba, in *Advances in the Synthesis and Reactivity of Solids*, Vol. 1, *Advances in the Synthesis and Reactivity of Solids*, edited by T. E. Mallouk (JAI Press Ltd., 1991), pp. 173-235.
78. B. Park, M. Nakata, S. S. Seomun, Y. Takanishi, K. Ishikawa, and H. Takezoe, Phys. Rev. E **59**, R3815 (1999).
79. J. G. Zhao, T. Yoshihara, H. W. Siesler, and Y. Ozaki, Phys. Rev. E **65**, 021710 (2002).
80. S. V. Shilov, H. Skupin, F. Kremer, T. Wittig, and R. Zentel, Phys. Rev. Lett. **79**, 1686 (1997).
81. Y. R. Shen, *The Principles of Nonlinear Optics* (Wiley, New York, 1984), pp. 67-87.
82. Y. G. Fokin, T. V. Murzina, O. A. Aktsipetrov, S. Soria, and G. Marowsky, Appl. Phys. B **74**, 777 (2002).

83. J. G. Zhao, T. Yoshihara, H. W. Siesler, and Y. Ozaki, Phys. Rev. E **64**, 031704 (2001).
84. A. L. Verma, B. Zhao, A. Bhattacharjee, and Y. Ozaki, Phys. Rev. E **63**, 051704 (2001).
85. C. V. Brown and J. C. Jones, Appl. Phys. Lett. **86**, 3333 (1999).
86. N. Vaupotic, V. Grubelnik, and M. Copic, Phys. Rev. E **62**, 2317 (2000).
87. A. A. Sigarev, J. K. Vji, R. A. Lewis, M. Hird, and J. W. Goodby, Phys. Rev. E **68**, 031707 (2003).
88. S. V. Shilov, H. Skupin, F. Kremer, T. Wittig, and R. Zentel, Macromol. Symp. **119**, 261 (1997).
89. Y. Nagasaki, T. Yoshihara, and Y. Ozaki, J. Phys. Chem. B **104**, 2846 (2000).
90. Y. Nagasaki and Y. Ozaki, Phys. Chem. Chem. Phys. **2**, 3037 (2000).
91. J. G. Zhao, K. Tatani, T. Yoshihara, and Y. Ozaki, J. Phys. Chem. B **107**, 4227 (2003).
92. 2Dshige© Shigeaki Morita, Kwansei-Gakuin University, 2004-2005. http://sci-tech.ksc.kwansei.ac.jp/~ozaki/

Appendix

Sample Preparations

The liquid crystal samples used in this study were prepared with standard processes. The sample preparations include several steps. In this section we will describe the processes in detail.

I. Sample Substrate Cleaning Procedure

The selections of substrates used to prepare a LC sample cell depend on the experimental requirements. To fulfill the conditions of IR spectroscopic measurements, the CaF_2 substrate coated with ITO conducting layer was used. If all the measurements are carried out by using the light source with the spectral range of UV-visible light, the ITO coated fused silica can be chose to prepare the sample cells. The substrate cleaning process is as the following steps:

1. Wash the substrates with the diluted liquid soap solution, than rinse the substrates with clean water.
2. Put the washed substrates into diluted liquid soap solution with ultrasonic vibration treatment for 15 min.
3. Put as treated substrates into deionized (DI) water with ultrasonic vibration treatment for 5 min.
4. Put as treated substrates into isopropyl alcohol with ultrasonic vibration treatment for 10 min.
5. Put as treated substrates into acetone with ultrasonic vibration treatment for 10 min.
6. Put as treated substrates into DI water with ultrasonic vibration treatment for 5 min. Replace fresh DI water and repeat this ultrasonic vibration treatment for three times.

7. Repeat steps 4 to 6 if necessary.
8. Rinse the as treated substrates with DI water and purge nitrogen gas with sufficient pressure to dry the substrates immediately.
9. Put the as treated substrates into clean oven, baking for 1hr in 100 °C.

II. Alignment Layer Preparation

The selection and treatment of the alignment material, depending on the design parameters of liquid crystal samples, decides the boundary properties of the liquid crystal thin film. For example, the pretilt angle, anchoring strength and residue charge effect on the surface of the alignment layer are all influenced with the alignment materials. The material selections also depend on the alignment methods. Up to now, many different alignment methods are still under developing. The most conventional alignment method is the rubbing treatment with polyimide materials. Photo alignments with UV definable material thin films and the ion-beam-processed diamond-like carbon thin film are two of the promising alignment layers. In this study, we use the rubbing method to produce the alignment effect on polyimide thin film. The polyimide material used here is RN1842 from Nissan chemical. The preparations of alignment layers are as followed:

1. Dilute the RN1842 with the solution in a concentration of 15% and wait for the temperature of the solution to be the same as the room temperature.
2. Put droplets of diluted RN1842 solution on the substrate surface. The amount of the material depends on the size of the substrate.
3. Coat the alignment layer with a spin coater. The spinning rate used for this material is set at 300 rpm for 5 sec and followed 2600 rpm for 25 sec. The spinning rate should be fine adjusted if the concentration of solution or the material is changed.
4. When the spin coating is finished, move the coated substrate immediately into an oven preset at 80 °C for soft baking for 10 min.

5. After the soft baking, the hard baking treatment of the coated thin film needs to be carried out with 250 °C for 1 hr.
6. Rubbing the alignment layer with rubbing machine. Set the rotation speed of the rubber at 1000 rpm. The distance between rubber and the substrate is about 0.2 mm, and the moving speed of the substrate is about 5 cm/min. The parameters of the rubbing treatment no doubt depend on the sample design.

III. Cell Assembly and Liquid Crystal Filling

The spacers used in our sample are small silicate balls. The diameter of the spacer which controls the cell gap is determined by the sample design. Since the cell gap should be very small to form an SSFLC sample, the spacer diameter was chose to be 1.5 or 2 μm.

1. The spacers are dispersed into a UV curable gel NOA65 with a volume concentration of about 5% by a mixer. The concentration should be adjusted according to the diameter of the spacer.
2. Laying the spacer with UV gel on the two sides of the substrate.
3. Assembly the substrates in desired direction to form a cell and adjust the cell gap to become uniform by adding a proper pressure on the substrates.
4. Expose the cell with UV light to cure the UV gel.
5. After the gel is cured, put the empty cell onto a hot plate. Raise the temperature to be above the clearing point of the liquid crystal material then hold at a fixed temperature within the isotropic phase of the liquid crystal.
6. Put several droplets of liquid crystal on the opening of the empty cell and wait the liquid crystal to be filled into the whole cell by capillary force.
7. Slowly cool down the cell to room temperature then seal the opening of

the cell with quickly dry gel.

8. Attach the wires with conducting copper tape.
9. If necessary, repeat the temperature raising and decreasing processes with applying a proper electric field to stabilize the as prepared sample.